JOURNAL OF GEOPHYSICAL RESEARCH, VOL. 95, NO. D11, PAGES 18,441–18,471, OCTOBER 20, 1990

Tropospheric OH in a Three-Dimensional Chemical Tracer Model: An Assessment Based on Observations of CH_3CCl_3

C. M. SPIVAKOVSKY, R. YEVICH, J. A. LOGAN, S. C. WOFSY, AND M.B. MCELROY

Division of Applied Sciences and Department of Earth and Planetary Sciences, Harvard University, Cambridge, Massachusetts

M. J. PRATHER

NASA Goddard Space Flight Center, Institute for Space Studies, New York

The three-dimensional global distribution of OH over a year is calculated as a function of temperature, ultraviolet irradiance, and densities of H_2O, CO, O_3, CH_4, and NO_t (defined as NO + NO_2 + NO_3 + $2N_2O_5$ + HNO_2 + HNO_4). The concentration of OH is computed within a chemical tracer model (CTM) with an accuracy comparable to that of a detailed photochemical model. Distributions of CO, NO_t, O_3, CH_4, and the density of O_3 column were specified on the basis of observations. Meteorological fields were derived from the general circulation model developed at the Goddard Institute for Space Studies. The numerical method for parametrization of chemistry is described in *Spivakovsky et al.* (this issue). The CTM is used to simulate the global distribution of CH_3CCl_3. The computed distribution of OH implies a lifetime of 5.5 years for CH_3CCl_3 (obtained by relating the global burden of CH_3CCl_3 to the global loss, integrated using simulated three-dimensional distributions). Analysis of the long-term trend in CH_3CCl_3 as defined by observations suggests a lifetime of 6.2 years (consistent with *Prinn et al.* (1987)), indicating that model levels of OH may be too high by about 13%. This estimate for the lifetime depends on industry data for global emissions and on the absolute calibration of observations. It is argued that seasonal variations of CH_3CCl_3 provide an independent test for computed OH fields that is insensitive to the uncertainties in the budget of CH_3CCl_3. The annual cycle of CH_3CCl_3 from about 25°S to the South Pole is dominated by seasonal changes in OH. Observed seasonal variations of CH_3CCl_3 indicate that the OH field south of 20°S±4° should be scaled by 0.75 ±0.25 from computed values, consistent with the result based on long-term trends. Reactions involving non-methane hydrocarbons were not included in the current model. These reactions could account for lower concentrations of OH than computed. Seasonal variations of CH_3CCl_3 in the tropics and in the northern mid-latitudes are dominated by effects of transport. If use of CH_3CCl_3 is phased out (as envisioned by the Montreal protocol), the dynamically driven seasonal variations of CH_3CCl_3 will decrease dramatically, whereas the chemically driven variations will remain proportional to the concentration of CH_3CCl_3; then the annual cycle of CH_3CCl_3 in northern mid-latitudes will provide a measure of OH as does at present the annual cycle in southern mid-latitudes. The influence of chemistry on the latitudinal distribution of CH_3CCl_3 is small and at present does not provide a constraint for the globally averaged OH or for the latitudinal distribution of OH. However, if emissions of CH_3CCl_3 were to cease, the tropical depression in the concentration of CH_3CCl_3 caused by high levels of OH in the tropics may provide an additional means to test OH models.

1. INTRODUCTION

The OH radical plays a critical role in the chemistry of the lower atmosphere. Reactions with OH provide the dominant path for removal of a variety of halocarbons, hydrocarbons, and CO, and for conversion of NO_2 to nitric acid. The global abundance of OH determines the atmospheric residence times for many industrial compounds, including those contributing to the destruction of the ozone layer and to the greenhouse effect. Because of the extreme variability of OH in time and space, one has to rely on models rather than on observations to provide the global distribution of OH. The concentration of OH is sensitive to the intensity of solar radiation, to temperature and to concentrations of H_2O, CO, O_3, CH_4, nitrogen oxides, and hydrocarbons. These quantities have to be measured simultaneously with the concentration of OH to provide a test for the kinetic equations describing the photochemistry. Such comparisons for a local environment [*Perner et al.*, 1987; *Platt et al.*, 1988], however important, do not accomplish the task of testing a global model for OH, which depends critically on the climatologies of cloud cover, ground albedo, temperature, water vapor, and trace gases.

Paper number 90JD01299.
0148-0227/90/90JD-01299$05.00

Observations of CH_3CCl_3 have been used to assess the globally and annually integrated concentration of OH [*Singh*, 1977*a*, *b*; *Lovelock*, 1977; *Makide and Rowland*, 1981; *Logan et al.*, 1981; *Chameides and Tan*, 1981; *Prinn et al.*, 1983, 1987; *Khalil and Rasmussen*, 1984*a*; *Fraser et al.*, 1986], since the reaction with OH provides the dominant sink for CH_3CCl_3, and the source of CH_3CCl_3 is documented by the industry [Midgley, 1989]. Recent systematic measurements of CH_3CCl_3 and other tracers such as chlorofluorocarbons (CFCs) [*Prinn et al.*, 1987; *Fraser et al.*, 1985*a*, *b*, 1987; *Cronn et al.*, 1986; *Cunnold et al.*, 1986] offer new possibilities for testing photochemical models. The major sources of CH_3CCl_3 and CFCs are located in the same industrial regions, but in contrast to CH_3CCl_3, CFCs are inert in the troposphere. Simulations of CH_3CCl_3 and CFCs used jointly may help separate the influence of chemistry and transport in determining the distribution of CH_3CCl_3. A three-dimensional chemical tracer model (CTM), with realistic representation of global circulation and chemistry, is essential for interpretation of measurements and for simulation of important features of the distributions.

Hunt and Manabe [1968], *Hunt* [1969], and *Cunnold et al.* [1975] were among the first to use general circulation models (GCMs) to study the global distribution of chemical tracers. *Mahlman and Moxim* [1978] greatly improved the flexibility and efficiency of computational methods for applications to passive tracers, species that are not expected to influence the circulation.

They introduced a CTM designed to run independently of the GCM using transport fields recorded in a prior GCM simulation. Subsequent work at GFDL and other laboratories examined global distributions of O_3 [*Mahlman et al.*, 1980; *Levy et al.*, 1985], N_2O [*Levy et al.*, 1982], CO [*Pinto et al.*, 1983], halocarbons [*Golombeck and Prinn*, 1986], NO_x ($NO + NO_2$) [*Levy and Moxim*, 1987, 1989], and CO_2 [*Fung et al.*, 1983]. These studies focused on the effects of transport, with the exception of the early study of CO which used monthly and longitudinal averages of concentrations of OH.

The present paper belongs to a series intended to develop a global CTM with realistic simulation of photochemistry as well as meteorology. The CTM uses transport fields from the GCM developed at Goddard Institute for Space Studies [*Hansen et al.*, 1983]; numerical algorithms for simulating advection are described by *Russell and Lerner* [1981] and *Prather* [1986]. The CTM has been used to study the global dispersion of species emitted mainly in industrialized regions at northern mid-latitudes, chlorofluorocarbons (CFCs) [*Prather et al.*, 1987], and ^{85}Kr [*Jacob et al.*, 1987]. Transport from continents to the oceans and ventilation of the boundary layer was tested in the simulation of the distribution of ^{222}Rn [*Jacob and Prather*, 1990; *Balkanski and Jacob*, 1990; *Balkanski et al.*, 1989].

The present study introduces the representation of tropospheric chemistry that allows for calculation of chemical reaction rates within a CTM simulation with the accuracy comparable to that of the detailed chemical model. (The numerical method for parametrization of chemistry is described by *Spivakovsky et al.* [this issue].) The CTM is described in section 2. The global distribution of tropospheric OH is calculated as a function of time, atmospheric composition, temperature, and solar irradiance (section 3). Sections 4-6 examine the options for testing the accuracy of computed fields for OH.

In section 4 we use observed temporal trends of CH_3CCl_3 [*Prinn et al.*, 1987] in order to evaluate the globally integrated OH concentration (weighted by frequency of reaction with CH_3CCl_3), assuming accurate knowledge of rates for emissions and the current absolute calibration of the observational data. We discuss a procedure, proposed by *Prinn et al.* [1987], that was intended to give an estimate of both the loss rate and the absolute calibration, for a given level of emissions. We show that a family of values for these parameters is consistent with presently available data for CH_3CCl_3 and conclude that in practice, one has to assume the absolute calibration in order to determine the loss rate of CH_3CCl_3.

Section 5 examines the feasibility of using the observed latitudinal distribution of CH_3CCl_3 as a test for computed concentrations of OH [cf. *Prinn et al.*, 1987]. Model results indicate that the latitudinal distribution of CH_3CCl_3 is determined primarily by transport, not by chemistry. We show that at present the latitudinal distribution of CH_3CCl_3 as defined by the ALE data provides little information on either the globally integrated OH concentration or on the distribution of OH with latitude.

Section 6 focuses on seasonal variations of CH_3CCl_3 as a potential test for computed concentrations of OH. Observations at middle latitudes display annual cycles that have been attributed to seasonal variations in atmospheric transport [*Prinn et al.*, 1983] and in the concentration of OH [*Khalil and Rasmussen*, 1984*b*; *Fraser et al.*, 1986]. Our analysis suggests that annual cycles of CH_3CCl_3 are controlled, or strongly influenced, by dynamical processes at latitudes northward of 25°S. We show that seasonal variations of CH_3CCl_3 at southern mid- and high- latitudes provide a test for computed concentrations of OH. The results of this test are insensitive to errors in absolute calibration or in the rates assumed for global emissions of CH_3CCl_3.

2. DESCRIPTION OF THE MODEL

2.1. *Dynamics*

The CTM solves the three-dimensional continuity equation for chemically reactive tracers. The dynamical module is described by *Prather et al.* [1987]. It uses wind fields, surface pressures, and convective mass fluxes recorded at 4-hour intervals from the GCM [Hansen et al., 1983]. The GCM has a resolution of 4° in latitude by 5° in longitude. Height is resolved into 9 layers using σ coordinates. The two highest layers reach into the stratosphere, extending from approximately 150 to 10 mbar. For the present study, transport fields derived from the 4°x5° GCM were averaged over spatial elements of 8° latitude by 10° longitude and into 8-hour time intervals. Advection was treated using the slopes method of *Russell and Lerner* [1981]. The simulation of the interhemispheric transport, examined previously using distributions of CFCs [*Prather et al.*, 1987] and ^{85}Kr [*Jacob et al.*, 1987], is tested further as discussed below.

2.2. *Chemistry*

The chemical module computes the change in tracer concentration due to chemical reactions during a time step. Rates of chemical production and loss vary spatially and temporally reflecting variations in background concentrations, temperature, and solar irradiance. The irradiance in turn is a function of cloudiness, surface albedo, solar zenith angle, and the density of the overhead ozone column. The chemical module is designed to use these quantities as input, with either prescribed fields or fields simulated by the CTM. In the present work, climatologies were specified for O_3, NO_t (defined as $NO + NO_2 + NO_3 + 2N_2O_5 + HNO_2 + HNO_4$), CO, CH_4, and ozone column using observations as described in Appendix A. Distributions of temperature, cloud cover, surface albedo, and water vapor were adopted from the GCM. Water vapor concentrations above 500 mbar were specified using observations, since concentrations of H_2O derived by the GCM for this altitude region are known to be too high (see Appendix A for details). The 24-hour average OH field was recalculated every 5 days.

In previous studies we used an efficient photochemical model to describe the chemistry of the troposphere [*Wofsy*, 1978; *Logan et al.*, 1978, 1981; *Prather et al.*, 1984]. If this model were used as a chemical module in the CTM, computation of the OH field for 1 year with a 5-day time step would take more than 50 hours of the CPU time on an Amdahl-V6 computer. Conceivably, for the present study the OH field could be computed once and then recycled within the CTM simulations, since there is no feedback between CH_3CCl_3 and OH. However, this approach would preclude the study of sensitivity of the computed field to concentrations of O_3, NO_t, CO, and H_2O, described in section 3. Furthermore, we intend to use the present model for simulations of CO, NO_t, and O_3, i.e., for studies requiring computation of chemical rates within the CTM simulation based on tracer distributions at a given time step.

In order to reduce the time required for computation of OH, we replaced the detailed chemical model with a set of explicit expressions describing the functional relationship between input parameters and the concentration of OH as computed in the full model [cf. *Dunker*, 1986; *Marsden et al.*, 1987]. We expressed the 24-hour average concentration of OH as a high-order polynomial in N independent variables including temperature, radiation conditions, and concentrations of O_3, NO_t, CO, and water vapor. The mathematical procedure for deriving the polynomials is described by *Spivakovsky et al.* [this issue]. As shown there, the polynomials represent tropospheric OH with the accuracy comparable to

that of the full chemical model. The computational cost, however, is reduced by more than a factor of 600. A simulation of 1 year for CH_3CCl_3 with the present CTM takes about 85 min on Amdahl-V6 with less than 5 min spent for computation of OH.

The procedure for determining stratospheric loss of CH_3CCl_3 is described in *Prather et al.* [1987]. Both the photodissociation of CH_3CCl_3 and its destruction by OH are treated as a first-order loss process. See Appendix B for more detail.

3. TROPOSPHERIC OH AS CALCULATED IN THE THREE-DIMENSIONAL MODEL

The zonally averaged distribution for tropospheric OH is shown as a function of latitude and pressure for four seasons in Figure 1 and Table 1. Concentrations are highest in the tropics and in mid-latitudes in summer. Elevated levels of O_3, NO_y, and H_2O in the northern hemisphere lead to the enhancement of OH, mitigated to some extent by higher concentrations of CO.

The shape of the vertical distribution of OH reflects mainly that of the rate of OH production by reaction

$$H_2O + O(^1D) \rightarrow 2OH \quad (1)$$

preceded by

$$O_3 + h\nu \rightarrow O_2 + O(^1D) \quad (2)$$

To a good approximation, the rate of (1) is proportional to the density of O_3, to the mixing ratio of H_2O, and to the ratio J/k, where J is the frequency of (2) and k is the mean rate constant for quenching $O(^1D)$ in reactions with N_2 and O_2 (weighted by mixing ratios of N_2 and O_2, respectively). The mixing ratio of water vapor decreases rapidly with height; the number density of O_3 has a maximum between 600 and 800 mbar; the J value, determined by the level of solar irradiance, increases with altitude under cloud-free conditions (see Appendix 3 by *Logan et al.* [1981]), and clouds amplify that effect by screening the troposphere below and scattering the photons upward; the corresponding increase with height in the ratio of J value over k is slightly offset by an increase in k, as a result of its dependence on temperature. These competing influences produce a maximum in the rate of OH production around 800 mbar. Frequencies of reactions with CO and CH_4 (major loss processes for OH) decline with height, resulting in a somewhat higher altitude, about 700 mbar, for the maximum in the concentration of OH than in the rate of production of OH.

The computed OH field exhibits significant seasonal variations in the subtropics, mid-latitudes, and subpolar regions, as shown in Figure 1. The monthly mean concentrations in excess of $10^6 cm^{-3}$ extend in the summer hemisphere from the equator to subpolar latitudes, while concentrations in the winter hemisphere are below $10^6 cm^{-3}$ poleward of 20°. Summer concentrations at 45° exceed winter concentrations by more than a factor of 5. The influence of

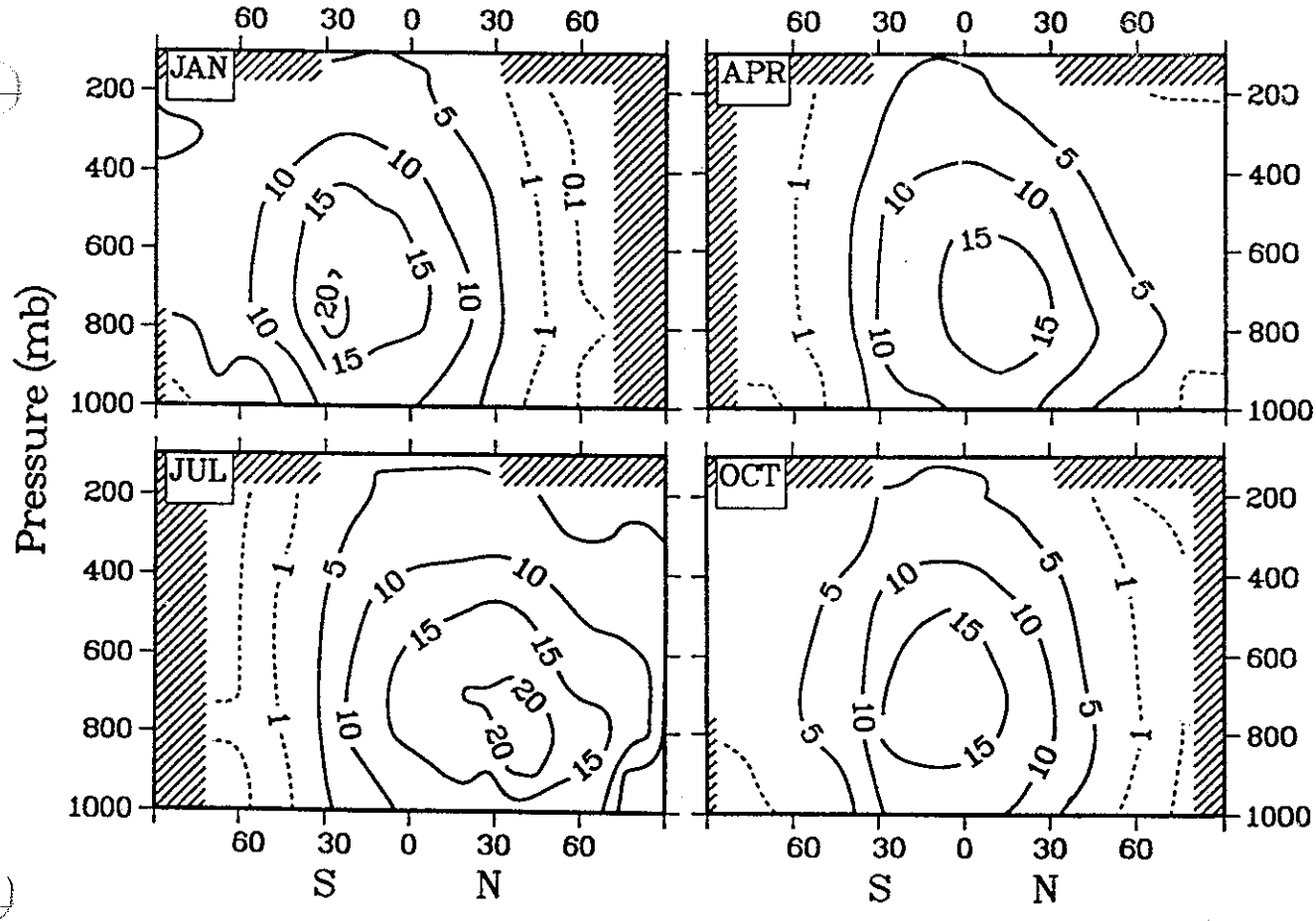

Fig. 1. Contours of tropospheric OH (units: 10^5 molecules cm^{-3}) calculated with the three-dimensional model and averaged zonally and monthly for January, April, July, and October. Solid contours are given with an increment of 5. The dashed lines represent 1 and 0.1. Shaded areas correspond to the domains where the calculation of OH was omitted, i.e., for the polar night regions, for the stratosphere or for altitudes below the surface (e.g., in Antarctica).

TABLE 1*a*. Zonally and Monthly Averaged Concentrations of OH for the Month of January

	1000 mbar	900 mbar	800 mbar	700 mbar	500 mbar	300 mbar	200 mb
90°N	...	...	...	...	...	...	...
84°N	...	...	...	...	...	...	...
76°N	...	...	...	...	...	...	...
68°N	0.047	0.049	0.10	0.075	0.039	0.017	1.1×10^{-5}
60°N	0.086	0.077	0.13	0.086	0.055	0.020	1.3×10^{-4}
52°N	0.15	0.26	0.54	0.49	0.41	0.17	0.052
44°N	0.45	0.97	1.5	1.3	1.1	0.48	0.18
36°N	1.4	2.4	3.1	2.9	2.4	1.3	0.57
28°N	3.6	4.9	7.5	7.6	5.7	3.0	2.2
20°N	6.5	7.9	11	11	7.6	4.4	3.2
12°N	7.9	10	13	13	9.4	5.4	4.2
4°N	9.6	12	15	16	13	6.7	5.0
4°S	11	13	16	18	15	7.9	6.1
12°S	9.8	13	16	17	15	9.0	7.9
20°S	12	15	19	20	17	9.8	8.1
28°S	12	17	22	21	18	9.6	8.2
36°S	8.3	11	16	17	15	8.1	7.5
44°S	5.3	7.0	13	14	13	7	6.9
52°S	3.5	4.7	11	12	10	6.1	6.2
60°S	2.5	3.2	8.5	9.2	7.7	5.4	5.5
68°S	2.5	6.2	9.6	9.4	6.9	5.1	5.9
76°S	1.0	2.3	4.5	7.7	6.1	4.7	6.1
84°S	0.11	1.6	4.0	7.5	5.9	4.5	5.9
90°S	...	...	...	6.8	5.7	4.6	5.3

Concentrations are given in 10^5 mol cm^{-3}.

TABLE 1*b*. Zonally and Monthly Averaged Concentrations of OH for the Month of April

	1000 mbar	900 mbar	800 mbar	700 mbar	500 mbar	300 mbar	200 mb
90°N	0.28	1.1	1.8	1.9	1.8	1.9	0.77
84°N	0.35	1.0	2.3	2.4	2.0	2.0	0.83
76°N	0.38	0.98	2.5	2.6	2.1	2.1	0.84
68°N	3.0	3.9	5.3	3.9	2.3	2.0	0.86
60°N	3.5	4.8	6.6	5.0	3.1	1.9	1.2
52°N	3.5	5.7	7.7	6.2	4.0	2.1	1.5
44°N	4.7	8.3	11	8.7	5.8	2.6	2.1
36°N	6.5	10	12	12	8.2	3.5	2.9
28°N	8.6	12	16	16	11	4.7	3.2
20°N	12	14	18	18	13	5.9	3.9
12°N	12	15	18	20	13	6.8	4.7
4°N	12	14	18	19	15	7.5	5.4
4°S	11	13	16	18	15	7.9	6.0
12°S	8.3	11	13	14	13	8.1	6.9
20°S	9.2	11	14	14	12	7.5	5.8
28°S	7.7	9.8	12	12	10	5.5	4.6
36°S	3.8	4.7	6.1	6.2	5.8	3.5	3.1
44°S	1.7	2.0	3.6	3.9	4.1	2.2	1.9
52°S	0.63	0.77	1.9	2.1	2.3	1.3	1.1
60°S	0.15	0.18	0.72	0.86	0.96	0.54	0.35
68°S	0.038	0.15	0.38	0.41	0.38	0.24	0.16
76°S	2.1×10^{-5}	3.2×10^{-4}	0.12	0.22	0.19	0.14	0.12
84°S	...	...	...	...	...	...	...
90°S	...	...	...	...	...	...	...

Concentrations are given in 10^5 mol cm^{-3}.

TABLE 1c. Zonally and Monthly Averaged Concentrations of OH for the Month of July

	1000 mbar	900 mbar	800 mbar	700 mbar	500 mbar	300 mbar	200 mb
90°N	1.1	3.0	4.7	4.7	7.3	4.8	3.6
84°N	3.4	4.9	11	11	9.0	5.4	4.4
76°N	2.9	4.3	11	11	9.3	5.4	4.3
68°N	9.5	13	17	13	8.8	4.6	4.0
60°N	10	14	17	14	9.7	4.4	4.1
52°N	9.4	16	19	16	12	5.2	4.4
44°N	12	20	24	20	14	6.3	5.1
36°N	13	19	22	21	16	7.4	6.1
28°N	10	14	19	20	17	7.8	5.5
20°N	13	16	19	20	15	7.6	5.9
12°N	12	15	18	19	15	7.4	5.5
4°N	11	13	17	18	14	7.3	5.4
4°S	10	12	16	17	13	7.2	5.3
12°S	7.8	11	14	14	11	6.9	5.1
20°S	6.7	8.2	11	11	9.1	5.6	3.7
28°S	4.7	5.9	7.5	7.6	6.4	3.4	3.0
36°S	1.7	2.1	2.6	2.7	2.7	1.4	1.3
44°S	0.56	0.66	1.1	1.3	1.5	0.71	0.62
52°S	0.14	0.16	0.42	0.51	0.62	0.29	0.21
60°S	0.057	0.040	0.12	0.093	0.093	0.040	0.0059
68°S	0.015	0.053	0.12	0.091	0.061	0.031	0.0046
76°S	...	...	...	...	...	...	...
84°S	...	...	...	...	...	...	...
90°S	...	...	...	...	...	...	...

Concentrations are given in 10^5 mol cm^{-3}.

TABLE 1d. Zonally and Monthly Averaged Concentrations of OH for the Month of October

	1000 mbar	900 mbar	800 mbar	700 mbar	500 mbar	300 mbar	200 mb
90°N	...	...	...	...	...	...	...
84°N	...	...	...	...	...	...	...
76°N	0.019	0.031	0.094	0.11	0.16	0.086	0.016
68°N	0.17	0.23	0.45	0.39	0.35	0.17	0.022
60°N	0.45	0.65	1.2	1.0	0.91	0.44	0.082
52°N	1.1	1.8	2.7	2.4	2.1	0.97	0.39
44°N	2.4	4.7	5.5	4.5	3.9	1.9	1.1
36°N	4.0	6.7	7.7	7.2	5.6	3.3	2.2
28°N	6.5	8.7	12	12	9.1	4.3	3.4
20°N	9.4	11	13	14	11	5.5	4.3
12°N	9.9	13	15	16	12	6.3	4.7
4°N	11	13	17	19	15	7.1	5.3
4°S	12	14	19	20	16	7.8	5.7
12°S	11	14	18	19	15	7.9	6.2
20°S	11	13	18	17	15	7.5	5.4
28°S	9.8	12	16	15	13	6.2	5.5
36°S	5.6	7.0	9.8	9.7	8.6	4.1	3.8
44°S	3.3	3.9	7.3	7.7	6.7	3.3	2.9
52°S	1.9	2.4	5.6	5.9	5.0	2.6	2.3
60°S	1.4	1.7	4.5	4.8	3.7	2.2	2.0
68°S	0.78	2.0	3.9	4.0	2.9	1.8	1.8
76°S	0.16	0.42	1.7	2.9	2.5	1.7	1.7
84°S	...	0.25	1.3	2.5	2.4	1.6	1.6
90°S	...	...	...	3.4	2.5	1.8	1.5

Concentrations are given in 10^5 mol cm^{-3}.

the seasonal variation in OH on the annual cycle of CH_3CCl_3 can be used to test computed concentrations of OH, as discussed in section 6.

The concentration of OH is significantly elevated over land, as illustrated in Figure 2. The upper panels show OH as a function of longitude and height in summer at 20°N and 20°S. Concentrations of NO_t, O_3, and CO are generally higher over land, reflecting anthropogenic and biogenic inputs. The lower panels show the concentration of OH computed using maritime values for NO_t, O_3, and CO throughout the globe. In that case as well, values for OH over land are higher than values over the ocean. About half of the land–ocean difference in OH concentration may be attributed to the higher surface albedo over land, with the remainder due to enhanced levels of NO_t and O_3 (compensated somewhat by higher levels of CO).

Our standard OH distribution corresponds to a global tropospheric mean concentration of 8×10^5 molecules cm^{-3} (integrated with respect to pressure from the surface to 100 mbar over the year). We examined the sensitivity of the calculated global mean OH to prescribed quantities by varying the assumed climatologies for NO_t, CO, O_3, and H_2O. If we assume maritime values for concentrations of NO_t, O_3, and CO over land, the calculated global mean abundance of OH decreases by 8%. A uniform increase of 25% in the concentrations of either water vapor or ozone results in an increase in OH by 10%. Inclusion of nonmethane hydrocarbons in the model is expected to lead to reductions in OH by 10–40% over the oceans, with reductions as high as 80% possible for the boundary layer over tropical continents (J. A. Logan, unpublished results, 1989). More precise estimates for the effects of hydrocarbons on global OH are not possible at present because of the scarcity of global data, especially for reactive alkenes [e.g., *Ehhalt et al.*, 1985; *Rudolph*, 1988; *Singh et al.*, 1988].

If we integrate loss of CH_3CCl_3 over the globe, and average over a year, we obtain a lifetime for CH_3CCl_3 of 5.5 years, about 10% longer than the value obtained by *Logan et al.* [1981]. The difference can be attributed partly to the change in kinetic data (the present study uses rate expressions recommended by NASA [1985]) and partly to the change in NO_x concentrations. The earlier model omitted peroxynitric acid (HO_2NO_2) as a component of NO_t due to uncertainty in the kinetic data at that time. In the upper troposphere, peroxynitric acid provides an important unreactive reservoir for odd nitrogen. Concentrations of NO_x, and thus OH, are consequently lower in the present model in the upper troposphere. In addition, current observations (Appendix A) suggest that concentrations of NO_x in southern mid-latitudes are lower than values used in the earlier study.

The concentrations of OH presented by *Crutzen and Gidel* [1983] are higher than our standard values at mid-latitudes in winter and at 0-2 km and at 8-12 km in summer (see Figure 3). They are lower in the tropics by as much as 60%. It is difficult to account for the differences based on known characteristics of the two models. To aid in resolution of such discrepancies in the fu-

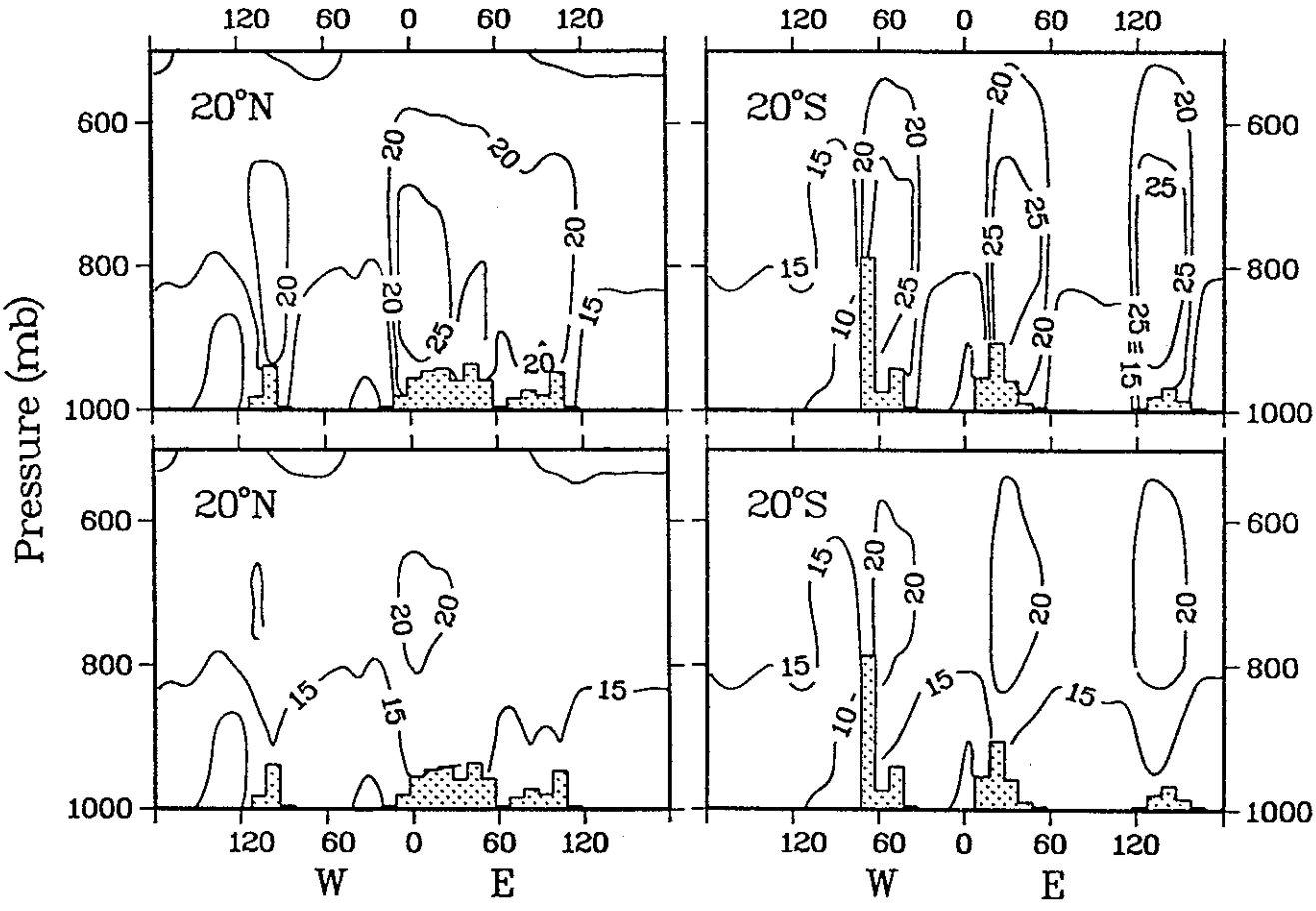

Fig. 2. Contours of tropospheric OH (units: 10^5molecules cm^{-3}) calculated with the three-dimensional model for two subtropical latitudinal bands 8° wide, centered at 20°. The lower panels show OH concentrations calculated with maritime values of NO_x, CO, and O_3 assumed throughout the globe.

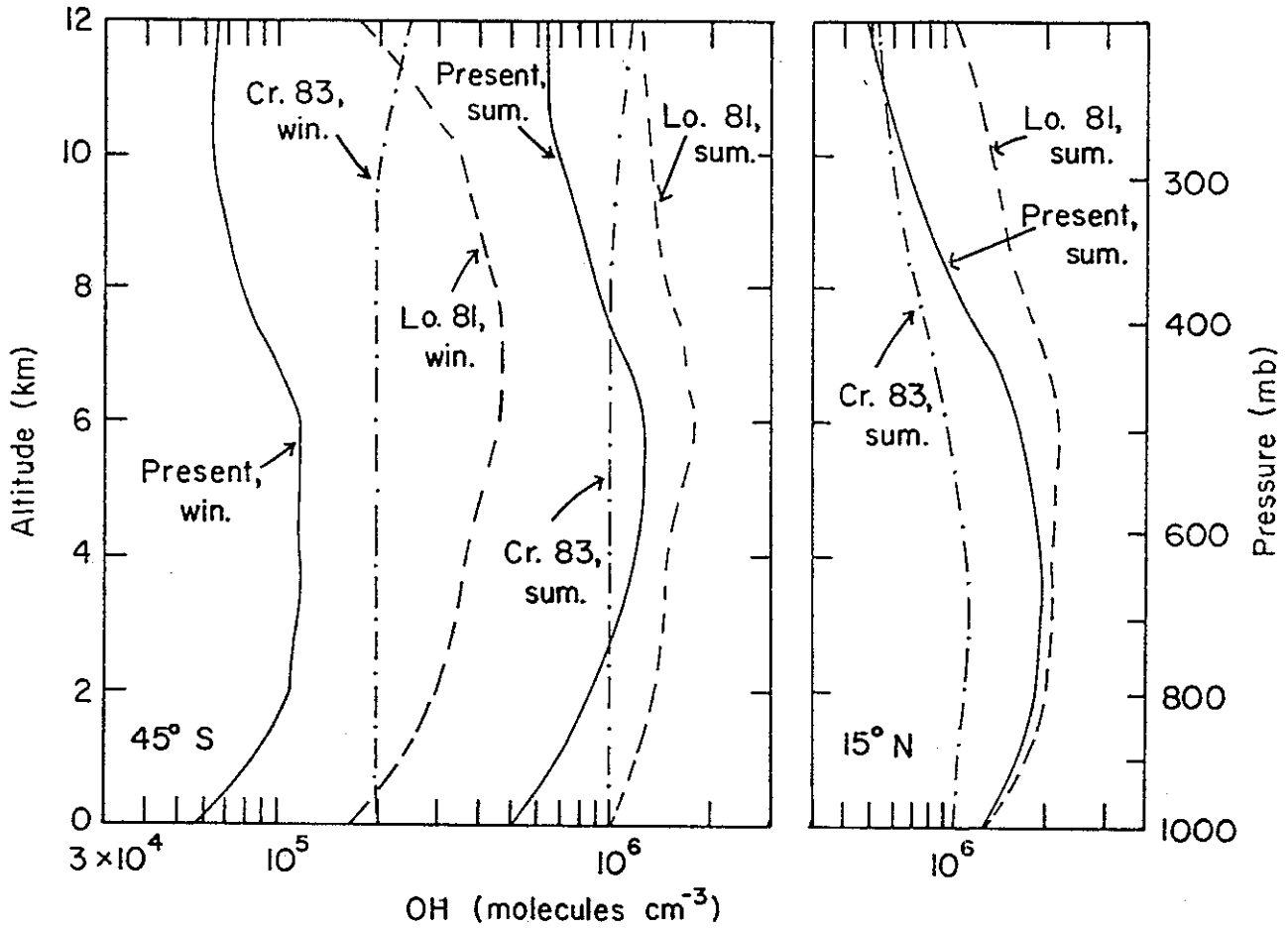

Fig. 3. OH concentrations for 45°S and 15°N in January and July, computed using the present full photochemical model (solid lines), and reported by *Crutzen and Gidel*, [1983] (dot-dashed lines), and by *Logan et al.* [1981] (dashed lines). The values reported by Crutzen and Gidel, which represent daylight averages, were rescaled to obtain 24-hour averages.

ture, we present information on rates for production and loss for the important reaction paths (see Table 2) in addition to concentrations of OH. The three-dimensional OH field from the present study (8° latitude by 10° longitude, for 7 and 9 vertical layers for the mid-latitudinal and tropical troposphere, respectively) computed with a 5-day time step for a year is available from the authors as ASCII files on the 5 1/4" floppy disks.

4. Global OH and Observed Trends in the Concentration of CH_3CCl_3

4.1. *Comparison With Observations*

Observed and calculated concentrations of CH_3CCl_3 at the five ALE/GAGE stations [*Prinn et al.*, 1987] are presented in Figure 4 (Atmospheric Lifetime Experiment and Global Atmospheric Gases Experiment). Rates of growth for the concentration of CH_3CCl_3, calculated with the standard OH model (solid lines) and with OH reduced by 25% (dashed lines), bracket the observed rates at all five stations. Lifetimes of CH_3CCl_3, computed as a ratio of global mass to global loss, for these simulations are 5.5 and 7.1 years, respectively. The best fit to the observed trends would be obtained for a lifetime of 6.2 years, corresponding to reduction of the standard OH concentrations by 13%.

The close agreement between model and observations must be regarded with caution, since the comparison depends on the absolute calibration of the observations and on the estimated magnitude of the global source. The absolute concentration of CH_3CCl_3 was revised by 20% from values initially reported [*Rasmussen and Lovelock*, 1983], and further adjustments can not be ruled out. It is likely that the global emission rate (Appendix B) has been underestimated, as discussed by *Khalil and Rasmussen* [1984*a*] and *Prinn et al.* [1983, 1987]. These authors quoted ranges for the lifetime of CH_3CCl_3 of 6±1.5 years and $6.9^{+1.2}_{-0.9}$ years, respectively, based on observed trends and available emission data. The latter estimate was obtained using the optimal estimation technique discussed below.

4.2. *Discussion of the Optimal Estimation Technique; A Budget Diagram*

It has been suggested by *Prinn et al.* [1987] that, given the source strength and a time series of observations, one can infer both a lifetime L and an absolute calibration factor F_c (a factor multiplying the currently accepted estimate of concentration in a calibration standard) for CH_3CCl_3. The procedure involves minimizing

$$S = \sum_{i=1}^{N} \left[\ln F_c + \ln o(t_i) - \ln c(c_o, t_i, L) \right]^2 \qquad (3)$$

with respect to L and F_c. Here $o(t_i)$ denotes the observed concentration at time t_i, N is the number of observations, and c_o denotes the initial condition. Concentrations $c(t_i)$ are computed using a

TABLE 2. Dominant Reactions for Production and Loss of OH

	15°N, summer at 4 km	44°S, summer at the surface	44°S, winter at 8 km
Production rates[a]:			
$O(^1D)+H_2O\rightarrow 2OH$	77.5	29.2	0.08
$HO_2+NO\rightarrow OH+NO_2$	22.3	2.8	0.90
$O_3+HO_2\rightarrow OH+2O_2$	17.2	7.4	0.43
$H_2O_2+h\nu\rightarrow 2OH$	15.6	3.8	0.10
$CH_3OOH+h\nu\rightarrow OH+CH_3O$	3.7	2.2	0.03
$HNO_4+h\nu\rightarrow OH+NO_3$			0.02
Total production (=loss)	136	45.3	1.57
Loss rates[a]:			
$OH+CO\rightarrow CO_2+H$	59.0	15.9	1.13
$OH+CH_4\rightarrow CH_3+H_2O$	26.8	14.1	0.20
$OH+CH_3OOH\rightarrow CH_3OO+H_2O$	12.6	4.7	
$OH+H_2CO\rightarrow HCO+H_2O$	9.2	2.6	
$OH+HO_2+M\rightarrow H_2O+O_2$	8.3	1.1	0.02
$OH+H_2O_2\rightarrow H_2O+HO_2$	6.4	0.98	
$OH+H_2\rightarrow H_2O+H$	6.3	3.8	0.04
$OH+O_3\rightarrow HO_2+O_2$	6.1	1.2	0.1
$OH+C_2H_6\rightarrow C_2H_5+H_2O$		0.66	
J values, s^{-1}:			
$O_3+h\nu\rightarrow O(^1D)+O_2$	1.38×10^{-5}	4.37×10^{-6}	6.25×10^{-7}
$NO_2+h\nu\rightarrow NO+O$	2.95×10^{-3}	1.78×10^{-3}	8.65×10^{-4}
Temperature, K	277	296	232
Air density, mol cm^{-3}	1.65×10^{19}	2.48×10^{19}	1.09×10^{19}
Concentrations:			
OH mol cm^{-3}	1.89×10^{6}	4.77×10^{5}	7.84×10^{4}
H_2O, mol/mol	6.60×10^{-3}	1.23×10^{-2}	1.93×10^{-4}
CO, ppbv	90	56	70
CH_4, ppbv	1700	1600	1600
O_3, mol cm^{-3}	5.83×10^{11}	3.87×10^{11}	4.69×10^{11}
NO_t, pptv	24	5.4	38
NO, mol cm^{-3}	7.16×10^{7}	1.80×10^{7}	4.23×10^{7}
NO_2, mol cm^{-3}	2.97×10^{8}	1.04×10^{8}	1.24×10^{8}
HO_2, mol cm^{-3}	1.67×10^{8}	9.66×10^{7}	7.99×10^{6}
CH_3OOH, mol cm^{-3}	1.11×10^{10}	1.64×10^{10}	2.50×10^{8}

[a] Units are 10^4 mol cm^{-3}. Rates are given for production and loss of OH over the ocean. Reactions contributing less than 1% to the production or loss of OH are not listed. All rates and concentrations are 24-hour averages. Results are from the full photochemical model [*Logan et al.*, 1981], updated to include HNO_4 in NO_t and to use rate coefficients from *NASA* [1985].

model to obtain values at individual stations, or global mean values, corresponding to observations $o(t_i)$.

However, this optimization problem appears to be ill posed. There is a continuum of near-optimal pairs (L, F_c) that correspond to values of S near the minimum. Figure 5, for example, shows the fit to the observed global trend provided by two such pairs, a lifetime of 10.6 years with a calibration factor 1.4 (solid line), and a lifetime of 6.2 years with a calibration factor of 1.0 (dashed line). Observations $o(t_i)$ are denoted by triangles. We used the global balance equation

$$\frac{dc}{dt} = p(t) - \frac{c(t)}{L} \tag{4}$$

as a model for $c(t_i)$, with the initial condition $c_o = o(t_1)\cdot F_c$. Here $p(t)$ denotes the emission rate at time t. Global mean concentrations $o(t_i)$ were computed from observations as described in the

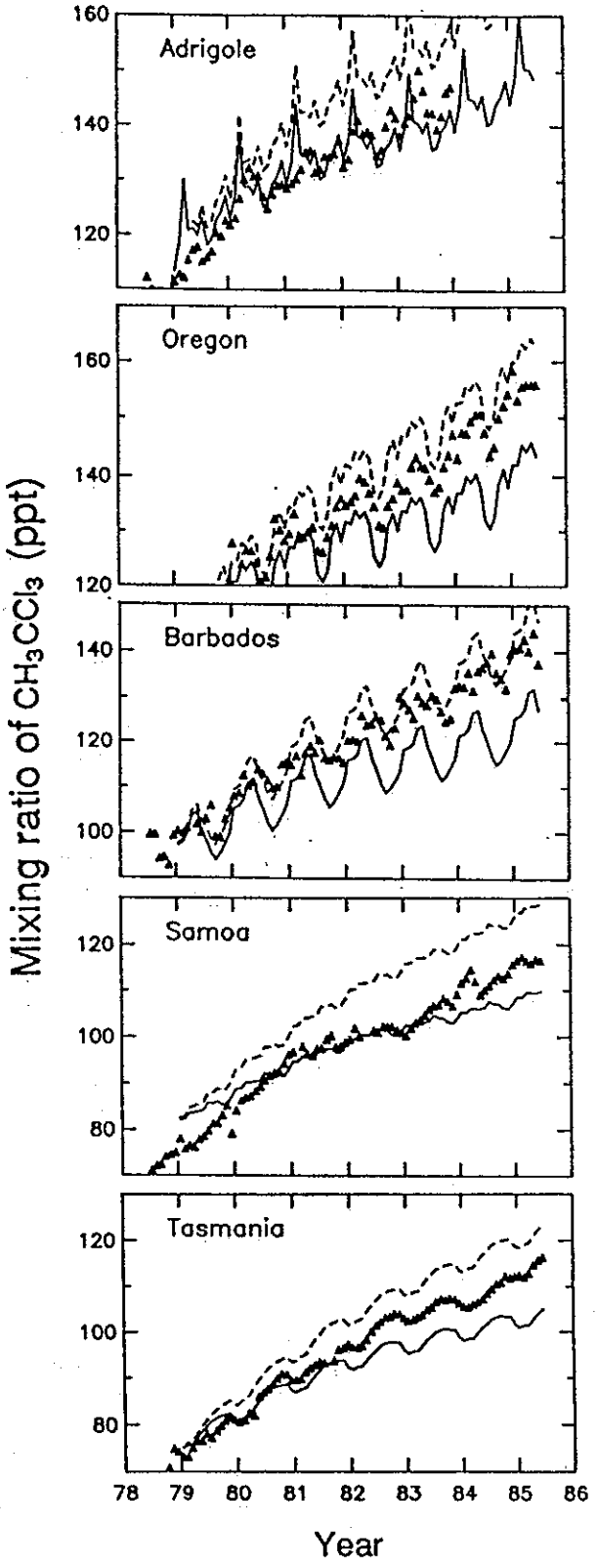

Fig. 4. Concentrations of CH_3CCl_3 (pptv) at the ALE sites. Observations (monthly means) are designated by triangles. Results of simulations are represented by monthly medians of surface concentrations calculated for a grid box containing the site [*Prather et al.* 1987]. Solid lines correspond to the simulation with the standard OH. Dashed lines correspond to the simulation with the standard OH reduced everywhere by 25%.

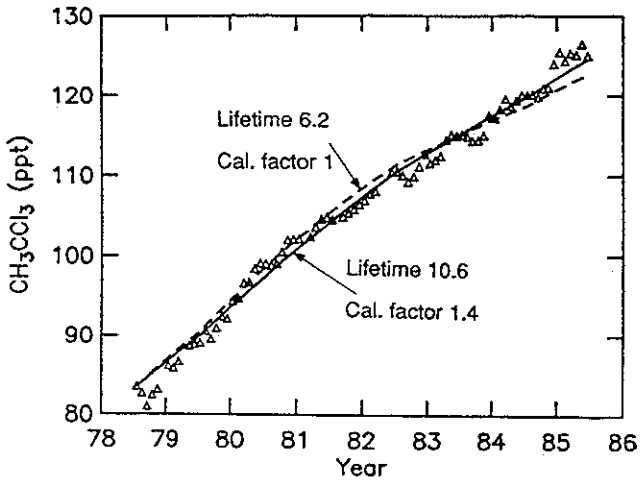

Fig. 5. Global trend in CH_3CCl_3. The vertical axis represents the global mean concentration, computed from (4), divided by the calibration factor. The solid line corresponds to the calculation with a lifetime of 10.6 years and a calibration factor of 1.4. The dashed line represents the calculation with a lifetime of 6.2 years and a calibration factor of 1. The values for the global burden o_i (triangles) were derived from reported monthly concentrations at the ALE sites using an empirical expression $o_i = [0.95(N_{Mi} + B_i + S_i + T_i)]/4$, where B, S, and T represent concentrations at Barbados, Samoa and Tasmania, respectively, and N_M is concentration at northern mid-latitudes taken as a mean of concentrations at Adrigole and Oregon. Before January 1980 and after December 1984, when only one of the two stations was operational, observations at that station were used as N_M. The global burden calculated by that expression is consistent with the three-dimensional model results (assuming that concentrations at the ALE sites are represented by monthly medians [*Prather et al.* 1987] for the appropriate grid boxes at the surface).

figure caption. Computed concentrations $c(t)$ were divided by the associated calibration factor, to allow comparison on the same scale.

Uncertainties in the absolute values of concentrations and emissions are closely related in the global balance, as may be seen by rewriting (4) as

$$\frac{dc}{dt} = \frac{F_p}{F_c} p(t) - \frac{c(t)}{L} \tag{5}$$

where F_p is a scaling factor for emissions. Figure 6 provides a simple diagram for estimating the lifetime should the magnitude of the source or the calibration standard be changed. After F_p/F_c is determined, an appropriate lifetime L is defined on the left-side vertical axis by a point on the solid curve (obtained by minimizing

$$\sum_{i=1}^{N} \left[o(t_i) - c(c_o, t_i, L) \right]^2$$

with respect to L). Here $c(c_o,t,L)$ is a solution of (5) with the initial condition $c_o = o(t_1)$. The root-mean-error of the fit σ is given by the dashed line, with values read from the vertical axis on the right side of Figure 6.

The results in Figure 6 are consistent with those discussed by *Khalil and Rasmussen* [1984*a*]. For the presently accepted calibration standard and emissions [*Khalil and Rasmussen*, 1984*a*; *Prinn et al.*, 1987], which correspond to $F_p = 1$ and $F_c = 1$, the best fit is obtained for a lifetime of 6.2 years. The dashed line in Figure 6, which for a given level of emissions relates σ to the cali-

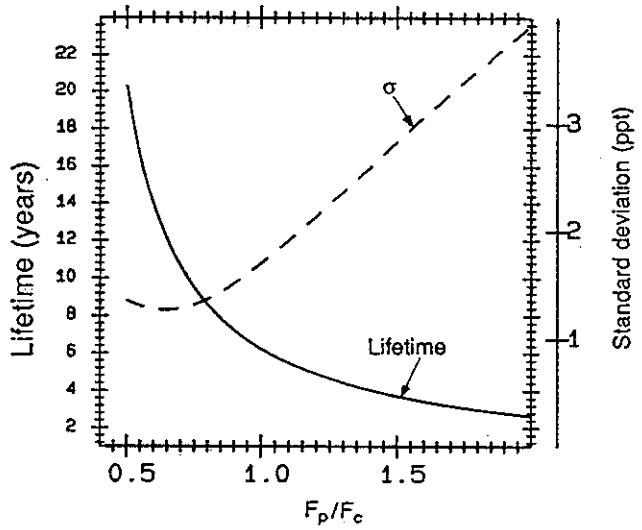

Fig. 6. Diagram for estimating the lifetime of CH_3CCl_3 for different levels of emissions and absolute concentration defined by the scale factors F_p and F_c with respect to the presently established values [*Prinn et al.*, 1987; *Khalil and Rasmussen*, 1984*a*]. For a given F_p/F_c, the lifetime of CH_3CCl_3 is defined on the vertical axis at the left hand side by a point on the solid curve. This value for lifetime L gives the least square fit of the solution for (5) to the time series of the mean global concentration (derived from observations using the formulae given for Figure 5). The corresponding root-mean-square error σ is represented by the dashed line scaled to the vertical axis on the right-hand side.

bration factor F_c, illustrates the difficulty in using observations as a constraint to determine both the lifetime and the calibration factor. For $F_p = 1$ lifetimes from 6 to 20 years, corresponding to calibration factors from 0.97 to 2, lead to essentially the same accuracy of the fit, with $\sigma = 1.5 \pm 0.25$ ppt.

5. THE LATITUDINAL DISTRIBUTION OF CH_3CCl_3: ROLES OF DYNAMICS AND CHEMISTRY

Figures 7 and 8 show computed global distributions for CH_3CCl_3 at the surface and at 500 mbar. The pattern is similar to that simulated for CFCs [*Prather et al.* 1987]. At the surface, closed contours distinguish source regions, with steep gradients in adjacent areas. In contrast, contours at 500 mbar show little indication of sources at the ground. Steep gradients are found at the surface also in the northern tropics indicating the northern limit of the intertropical convergence zone (ITCZ). North-south transport is inefficient in the lower troposphere in this region. The vertical profile is inverted to the south of the ITCZ, with higher concentrations aloft, reflecting the fact that southward interhemispheric transport takes place primarily in the upper troposphere [cf. *Plumb and McConalogue*, 1988; *Prather et al.*, 1987].

The model indicates that concentrations over large areas of the North Atlantic should be significantly higher than those over the North Pacific. Observations show a similar difference [*Prinn et al.*, 1987] between background concentrations observed at Adrigole (Ireland, 52°N, 10°W) with those for Cape Meares (Oregon, 45°N, 124°W). The model results suggest that large-scale transport patterns contribute to the higher background level for concentrations at Adrigole. Polluted air is advected to the North Atlantic from North American sources in spring and winter, and from European sources in summer (see Figure 7). The North Pacific is coupled less directly to source regions.

Figure 9 compares annual averages of observed (triangles) and simulated (circles) concentrations of CH_3CCl_3 at the ALE stations for 1979-1984. Concentrations are presented as increments with respect to the concentrations at Tasmania (41°S, 145°E), to remove a temporal trend in concentration. Some uncertainty is associated with interpretation of model results at the ALE sites north of the equator, in the regions with steep horizontal gradients (see Figure 7). The horizontal grid used in the CTM cannot resolve concentration differences along these gradients to better than 2-3 ppt, and uncertainty of comparable magnitude arises from exclusion of "polluted events" in the computation of background concentrations at the ALE stations in the model. In the ALE/GAGE program, the influence of pollution at Adrigole was identified by noting occasions when the concentration of short-lived industrial tracers was unusually high; samples exceeding a certain threshold were excluded from the computation of monthly means in defining the background [*Prinn et al.*, 1987; *Cunnold et al.*, 1986]. A similar procedure may be implemented in simulations by introducing a short-lived tracer emitted in industrialized areas, if the additional effort appears warranted. At present, we use a simple method to compute monthly mean "background" concentrations for the model at ALE sites taking the monthly median (50th percentile) to represent the background level [cf. *Prather et al.*, 1987]. This approach rests on two assumptions: (1) the median is not significantly affected by pollution events; and (2) the mean and median values coincide in "unpolluted" air. The annual mean computed from monthly medians is lower than the annual mean of monthly averages by 2-3 ppt for Adrigole, and by less than 1 ppt for other ALE stations.

Model results exhibit a change in the latitudinal gradient in the tropics associated with a zone of sluggish southward transport at low altitude. The model places this zone just north of the ALE site at Barbados at 13°N, 59°W (Figure 9), while observations suggest that this zone lies south of Barbados. According to the model, the location of this zone varies significantly with longitude (Figure 7), but there are no data available to test this feature. Apart from the discrepancy at Barbados, the model reproduces well the latitudinal distribution of CH_3CCl_3 as defined by the ALE data. The agreement between observed and simulated latitudinal distributions of CH_3CCl_3 shows that the parameterization of unresolved, presumably mesoscale, mixing, introduced by *Prather et al.*, [1987] and *Jacob et al.* [1987] in simulations of CFCs and ^{85}Kr, is also consistent with observations of CH_3CCl_3. The latitudinal gradient of CH_3CCl_3 (see Figure 9) remained essentially constant from 1979 to 1985, because the release rates changed little over that period (±8%) [cf. *Prather et al.*, 1987].

Prinn et al. [1987] used the observed latitudinal gradient of CH_3CCl_3 to constrain the lifetime of CH_3CCl_3 to $6.0^{+1.4}_{-1.0}$ years. Our analysis suggests that the latitudinal gradient of CH_3CCl_3 is determined primarily by transport, not by chemistry [cf. *Plumb and McConalogue*, 1988]. The concentration of OH has only a small influence on the latitudinal distribution of CH_3CCl_3, as shown in Figure 10. The curves represent zonal means, averaged over 6 model years (1979–1984), for (1) standard OH (solid line); (2) no tropospheric loss (dashed line); (3) uniform loss rate equal to the globally and annually averaged tropospheric loss rate for standard OH (dot-dashed line). The difference between these simulations is less than 5 ppt at any latitude. The difference between the solid and dot-dashed curves (with the maximum of less than 3 ppt at the equator) reflects the influence of the tropical bulge in the concentration of OH, and thus in the loss frequency of CH_3CCl_3, as compared to the globally uniform loss frequency. In the model the zonally and annually averaged lifetime of CH_3CCl_3 in the tropical lower troposphere (below 700 mbar) ranges from 2 years at the equator to about 4 years at 30°S and 3 years at 30°N.

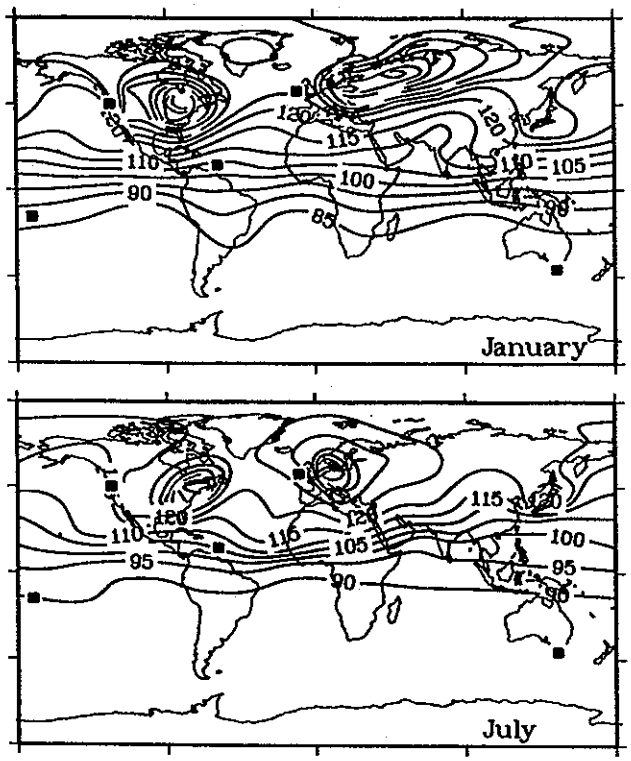

Fig. 7. Global distribution of CH_3CCl_3 in pptv at the surface for January and July of 1980. Locations of the ALE/GAGE sites are denoted by solid squares.

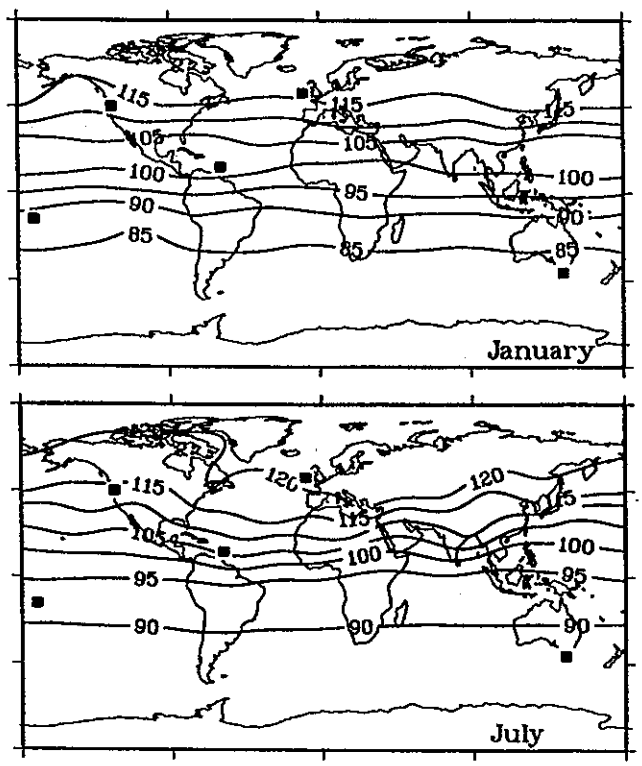

Fig. 8. Global distribution of CH_3CCl_3 in pptv at 500 mbar for January and July of 1980. Locations of the ALE/GAGE sites are denoted by solid squares.

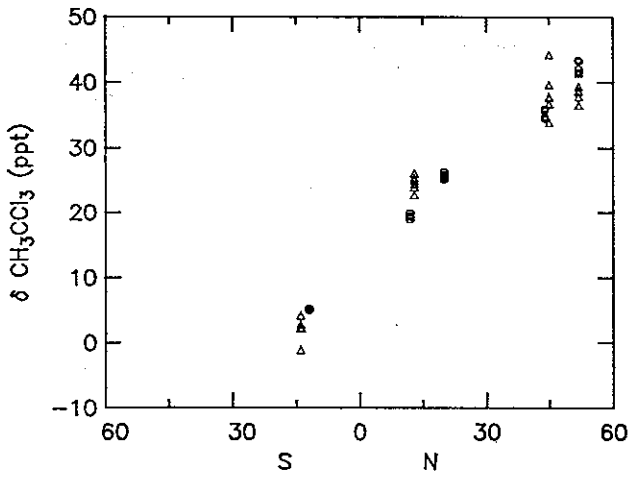

Fig. 9. Latitudinal distribution of CH_3CCl_3 in pptv as defined by annual means for ALE observations (triangles) and the CTM simulations at ALE sites (circles). The vertical axis represents the concentration in excess of that at Tasmania.

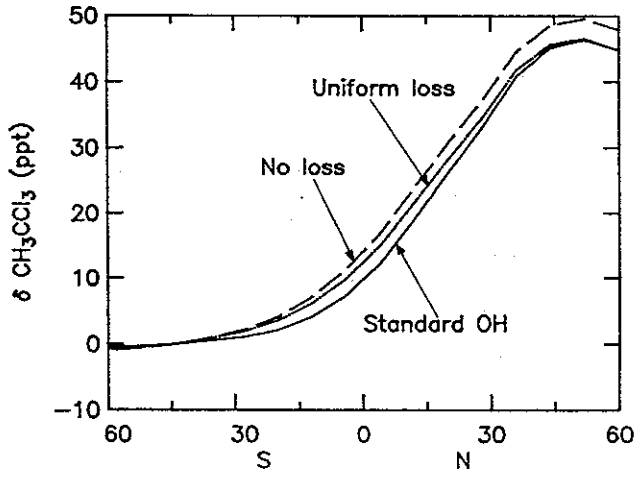

Fig. 10. A 6-year mean for zonally averaged concentrations computed using the CTM with the standard OH (solid line), with the uniform loss rate that is equal to the standard loss rate averaged annually and globally (dot-dashed line), and with no tropospheric loss (dashed line). The vertical axis represents the concentration in excess of that for the model zone 8° wide centered at 44°S (containing Tasmania).

Results in Figure 10 show that the local lifetime of CH_3CCl_3 in the tropics is not sufficiently short, as compared to the time for meridional mixing, to allow for a substantial impact of the latitudinal distribution of OH on that of CH_3CCl_3.

The influence of chemistry on the latitudinal distribution of CH_3CCl_3 (Figure 10) is smaller than interannual variations (Figure 9), and comparable to longitudinal variations (Figure 7). It is doubtful that the latitudinal distribution of CH_3CCl_3 could provide a meaningful constraint on the global distribution or global abundance of OH while the emissions of CH_3CCl_3 continue. If they were to cease (as envisioned by the Montreal protocol), the interannual variation in the northern hemisphere would drastically decline. Then, perhaps, the proposition of using the latitudinal distribution of CH_3CCl_3 as a test for OH should be reexamined. Finer latitudinal resolution of observations and special care in maintaining consistent calibration would be required.

6. ANNUAL CYCLES OF CH_3CCl_3 AND CFCs: ROLES OF DYNAMICS AND CHEMISTRY

Annual cycles for CH_3CCl_3 have been observed at mid-latitudes and attributed to seasonal variations in either atmospheric transport [*Prinn et al.*, 1983] or OH [*Khalil and Rasmussen*, 1984*b*]. *Fraser et al.* [1986] studied the annual cycle observed at Tasmania (41°S, 145°E) and assessed the relative contributions of chemistry and transport using a two-dimensional model. They compared seasonal variations computed in two model runs with: (1) the OH field from *Crutzen and Gidel* [1983] and the temperature field from observations; and (2) the annual means for OH and temperature in each grid box. They concluded that the seasonal variations of CH_3CCl_3 at Tasmania reflect "a combination of seasonality in transport and OH levels, with the latter being a dominant influence." The accuracy of their dynamical model in reproducing the seasonality in transport (e.g., for inert tracers such as CFCs) was not investigated, however.

In this section we compare observed and simulated seasonal variations for CH_3CCl_3 at all sites for which there are sufficient data to define the annual cycle (section 6.2). Observations of CFCs are used to confirm the accuracy of the model in reproducing the dynamical component of the annual cycle. We show that the seasonal variation of OH is the dominant influence on the annual cycle of CH_3CCl_3 south of about 25°S, and we use observed seasonal variations of CH_3CCl_3 to estimate the accuracy of the computed OH field. This assessment proves to be insensitive to uncertainties in either absolute calibration or in the magnitude of the source, as shown in section 6.1. In section 6.3 we discuss processes that in the model determine annual cycles of CH_3CCl_3 and CFCs. We begin by outlining the techniques used here for the study of seasonal variations.

6.1. *Numerical Concepts Used in the Analysis of Seasonal Variations*

The annual cycle of a gas is represented by the average concentration for each month, over the length of the record. Prior to averaging, a long-term trend is removed [*Fraser et al.*, 1986; *Enting*, 1987; *Pearman and Beardsmore*, 1984; *Thompson et al.*, 1986]. Methods for defining the long-term trend vary from one study to another [*Chatfield*, 1984; *Durbin*, 1963], but the differences are inconsequential as long as the residuals compose a stationary time series, with mean values for individual years close to zero.

We define a time-dependent concentration c_{trend} incorporating variations with periods longer than a year as

$$c_{trend}(t) = q_n(t) + f(t) \tag{6}$$

where t is in years, $q_n(t)$ is a polynomial, and $f(t)$ is given by

$$f(t) = \sum_{k=1}^{N-1} \alpha_k \cos\left(\frac{2\pi kt}{N}\right) + \beta_k \sin\left(\frac{2\pi kt}{N}\right) \tag{7}$$

for a data record of N years. First, the coefficients of $q_n(t)$ are defined using the least squares fit to the time series; the degree n is chosen as the highest for which the best fit polynomial is void of inflection points within the span of the record. The coefficients α_k, β_k in $f(t)$ are then chosen to give the least squares fit to the residuals obtained by subtracting $q_n(t)$ from the time series. The function $f(t)$ accounts for variations with frequency 1 through (N-1) cycles over the span of the record, and $q_n(t)$ represents those with frequencies lower than half a cycle per N years.

The definition of a c_{trend} used here guarantees that the sum of residuals $[c(t)-c_{trend}(t)]$ is equal to zero for the entire record, but not for an individual year. We evaluate the deviation of c_{trend} from an ideal baseline by the magnitudes of the ratios $R = S_{tr}/\sigma_{tr}$ where S_{tr} is a sum of the residuals for an individual year, and σ_{tr} is a square root of the variance (with respect to c_{trend}) over the span of the record. The magnitude of R does not exceed 0.2 for any data analyzed in this study, and most commonly is less than 0.1. It can be shown easily that $\sum_{i=0}^{N-1} f(t+i) \equiv 0$, i.e., the mean annual cycle would not change if the function $f(t)$ were not included in the definition of c_{trend}. However, values of $|R|$ would be larger. The functional form for c_{trend} is sufficiently flexible to give a good fit without artificially distorting the annual cycle. Coefficients of the polynomials $q_n(t)$ for all observations analyzed in this study are given in Table 3.

The mean deviations of the data from c_{trend} must be examined for statistical significance, since superposition of random variations will in general produce nonzero mean residuals. The statistical significance of an annual cycle may be assessed using a correlogram (i.e., the autocorrelation coefficient plotted against the time lag [*Chatfield*, 1984]). A sinewave-like pattern with the frequency of 1 cycle per year is characteristic of correlograms for the time series describing seasonally varying processes. Autocorrelation coefficients for a random time series of N independent observations are expected to be smaller than $\delta = 2/\sqrt{N}$ for 95% of time lags. An annual cycle is not considered significant at the 95% level unless the autocorrelation coefficient exceeds δ for a time lag of 12 months.

Figure 11 illustrates an application of this test. The upper panel shows the average of the residuals by month over the span of the record, for two time series, CFC-11 at Tasmania (5880 P) (asterisks) and CH_3CCl_3 at Samoa (diamonds). Monthly residuals have similar magnitudes at the two stations. However, the corresponding correlograms (lower panel) show that the annual cycle is not statistically significant for CH_3CCl_3 at Samoa, while there is a well defined annual cycle for CFC-11 at Tasmania. Correlograms for all time series of observations used in this study are given in Figure 12.

In section 6.2 we show that seasonal variations of CH_3CCl_3 at southern mid-latitudes are determined mainly by oscillations in the loss rate. The amplitude A_{abs} of these variations when measured in absolute terms (e.g., pptv), is a function of the absolute concentration of CH_3CCl_3, and thus, for the computed concentration, a function of the calibration standard and rates for emissions and chemical loss, as shown in Figure 13*a*. In contrast to A_{abs}, the amplitude A_{rel} of variations in the ratio $[c(t)-c_{trend}(t)]/c_{trend}(t)$, is insensitive to the assumed strength of the source and absolute calibration (Figure 13*b*). We assess the accuracy of the computed loss rate for CH_3CCl_3, and thus the accuracy of the computed OH, by comparing the variations in $[c(t)-c_{trend}(t)]/c_{trend}(t)$ as observed and simulated.

6.2. *Comparison of Observed and Simulated Annual Cycles*

We examine the relative importance of chemistry and transport in the annual cycles of CH_3CCl_3 by comparing model simulations for three tracers: 1) MCL/OH: CH_3CCl_3 with the loss frequency calculated on the basis of the standard OH; 2) MCL/50%OH: CH_3CCl_3 as in MCL/OH, but with OH everywhere divided by 2; and 3) MCL/ASEAS: a contrived tracer, identical to CH_3CCl_3 in all but one respect: the associated loss frequency in each grid box is at all times equal to the annual mean for the box in the simulation with the standard OH. Model runs were performed using two

TABLE 3. Coefficients of the Least Squares Fit Polynomials $q_n(t) = \sum_{i=0}^{n} a_i t^i$ for Time Series of Observations

Species	Location	Instrument	$a_0 x10^{-2}$, pptv	$a_1 x10$, pptv·month^{-1}	$a_2 x10^3$, pptv·month^{-2}	$a_3 x10^5$, pptv·month^{-3}	$a_4 x10^6$, pptv·month^{-4}	Time span
CH_3CCl_3	Tasmania	5880	1.04	-3.50	5.40	...	...	Jan. 1982 to Dec. 1985
CH_3CCl_3	Tasmania	5840	0.625	9.24	4.31	...	...	May 1980 to April 1984
CFC-11	Tasmania	5840 P	1.39	8.95	-1.35	...	...	July 1978 to June 1985
CFC-11	Tasmania	5840 S	1.38	8.79	-1.10	...	...	July 1978 to June 1985
CFC-11	Tasmania	5880 P	1.68	0.094	5.03	...	...	Jan. 1982 to Dec. 1985
CFC-11	Tasmania	5880 S	1.55	3.40	3.38	...	...	Jan. 1982 to Dec. 1984
CFC-11	Tasmania	5880 S	1.40	4.99	7.69	-5.12	...	Jan. 1983 to Dec. 1985
CFC-11	Tasmania	5880 S	1.33	10.9	-3.44	0.951	...	Jan. 1982 to Dec. 1985
CFC-12	Tasmania	5840	2.37	12.9	1.10	...	...	Jan. 1981 to Dec. 1984
CFC-12	Tasmania	5880	2.69	5.06	5.76	...	...	Jan. 1982 to Dec. 1985
CH_3CCl_3	Palmer	5880	0.695	10.4	-3.93	...	...	Aug. 1982 to July 1985
CH_3CCl_3	Oregon	5840	1.39	-16.6	60.2	-77.2	3.71	Jan. 1980 to Dec. 1984
CFC-11	Oregon	5840 P	1.75	1.48	4.86	...	...	July 1980 to June 1983
CFC-11	Oregon	5840 S	1.72	1.56	6.26	...	...	July 1980 to June 1983
CFC-12	Oregon	5840	2.59	16.2	-3.46	...	...	Jan. 1981 to Dec. 1982
CH_3CCl_3	Adrigole	5840	1.01	9.98	-5.43	...	...	Jan. 1979 to Dec. 1983
CFC-11	Adrigole	5840 P	1.60	8.28	-1.42	...	...	July 1978 to June 1983
CFC-11	Adrigole	5840 P	1.60	8.28	-1.42	...	...	July 1978 to June 1983
CFC-11	Adrigole	5840 S	1.60	8.24	-1.63	...	...	July 1978 to June 1983
CFC-12	Adrigole	5840	2.62	16.7	-3.58	...	...	July 1978 to June 1983
CH_3CCl_3	Barbados	5840	0.911	6.48	-1.09	...	...	July 1978 to June 1985
CFC-11 P	Barbados	5840	1.51	8.76	-1.69	...	...	July 1978 to June 1983
CFC-11 S	Barbados	5840	1.53	7.58	1.32	...	...	July 1978 to June 1983
CFC-12	Barbados	5840	2.59	12.1	1.54	...	...	Jan. 1979 to Dec. 1982
CH_3CCl_3	Samoa	5840	0.661	8.31	-3.13	...	...	July 1978 to June 1985
CFC-11	Samoa	5840 P	1.38	10.4	-3.28	...	...	Jan. 1979 to Dec. 1982
CFC-11	Samoa	5840 S	1.39	10.4	-3.64	...	...	Jan. 1979 to Dec. 1982
CFC-12	Samoa	5840	2.36	17.7	-5.90	...	...	July 1978 to June 1983

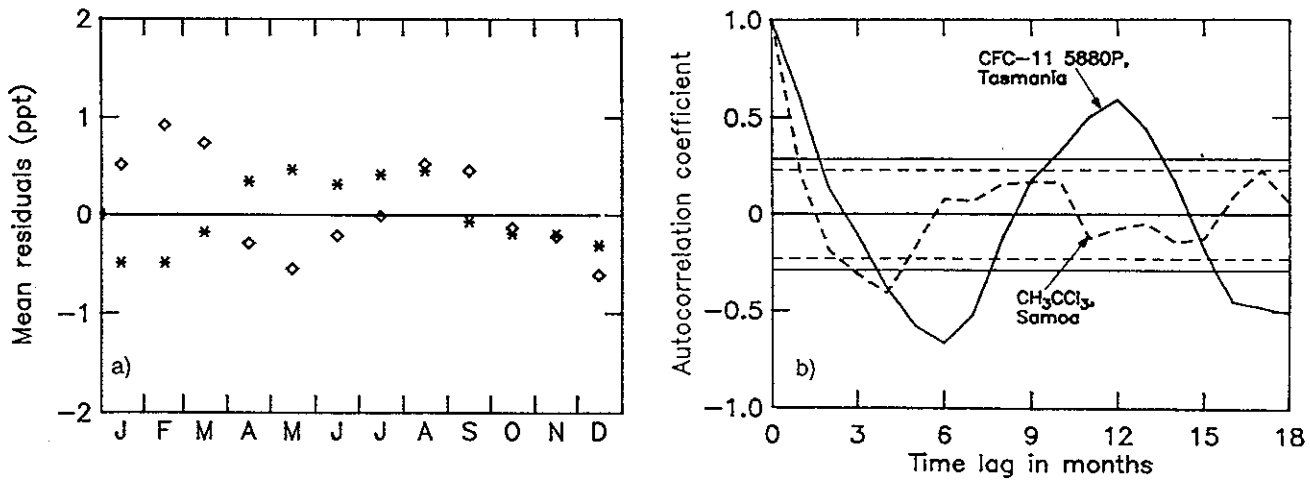

Fig. 11. Recurring seasonal variations vs. random variations. (*a*) Monthly deviations from c_{trend} (as defined in section 6.1) averaged over the length of the record, for CFC-11 (5880 P) at Tasmania (asterisks) [*Fraser et al.*, 1985*a*, 1987] and for CH_3CCl_3 at Samoa (diamonds) [*Prinn et al.*, 1987]. (*b*) Correlograms for CFC-11 and CH_3CCl_3 (solid and dashed lines, respectively). Associated thin horizontal lines (solid and dashed lines for CFC-11 and CH_3CCl_3, respectively) denote a 2σ (i.e., $2/\sqrt{N}$) range. The autocorrelation coefficients for a time lag of 12 months are 0.8 for CFC-11 and −0.1 for CH_3CCl_3. As explained in section 6.1, variations for different years appear to be significantly correlated for CFC-11 and noncorrelated for CH_3CCl_3.

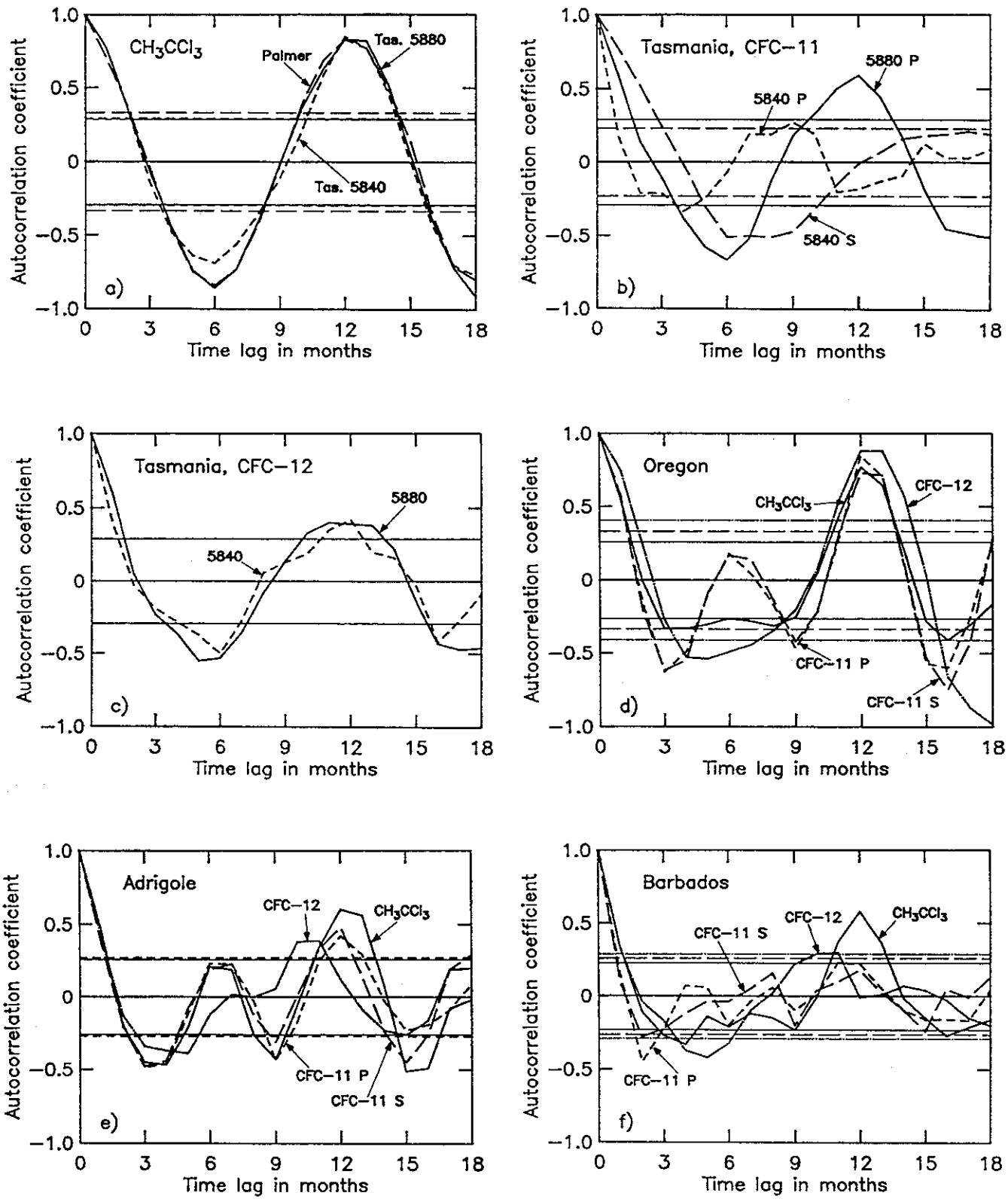

Fig. 12. Correlograms for time series of observations: (a) CH_3CCl_3 at Tasmania (solid and short-dashed lines for the 5880 and 5840 instruments, respectively, [*Fraser et al.*, 1985*a*, 1987]) and Palmer Station (long-dashed line, [*Cronn et al.*, 1986]); (*b*) CFC-11 at Tasmania (solid, short-dashed and long-dashed line for 5880 P, 5840 P and 5840 S, respectively, [*Fraser et al.*, 1985*a*, 1987]); c) CFC-12 at Tasmania (solid and dashed line for 5880 and 5840, respectively [*Fraser et al.*, 1985*a*, 1987]); correlograms for (*d*) Oregon, (*e*) Adrigole, (*f*) Barbados, and (*g*) Samoa are denoted by a solid line for CH_3CCl_3, dot-dashed line for CFC-12 and short- and long-dashed lines for CFC-11 P and S, respectively [*Prinn et al.*, 1987, *Cunnold et al.*, 1986]. Associated thin horizontal lines denote the 95% confidence interval as in Figure 11.

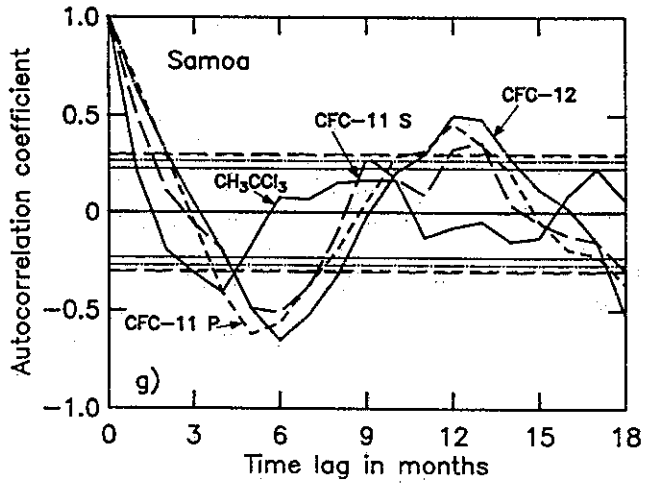

Fig. 12. (continued)

sets of winds, convection frequencies, etc., obtained from two successive years of the GCM, denoted FSD and SSD for the first and second set of dynamics, respectively.

6.2.1. *Southern mid-latitudes.* Figure 14 shows observed and simulated annual cycles of CH_3CCl_3 at Tasmania [*Fraser et al.*, 1985, 1987] and at Palmer Station [*Cronn et al.*, 1986]. Monthly mean values derived from observations are designated by crosses and circles for measurements with the HP-5840 and HP-5880 instruments, respectively. The annual cycles for these observations are highly significant, as shown by the strong peak at 12-13 months in the associated correlograms (Figure 12*a*).

The solid and dot-dashed lines in Figure 14 represent simulations of CH_3CCl_3 with standard OH (MCL/OH) and with OH divided by 2 everywhere (MCL/50%OH). The dashed lines correspond to MCL/ASEAS, showing the annual cycle produced by variations in atmospheric transport alone, and the difference between the MCL/OH and MCL/ASEAS represents the effect of seasonality in the loss rate. The model accurately reproduces the annual cycle of CH_3CCl_3 observed at both Tasmania and Palmer Station. The amplitude for MCL/ASEAS is about three times smaller than for MCL/OH. Thus in agreement with *Fraser et al.* [1986] we find that seasonal variations in OH dominate the simulated annual cycle of CH_3CCl_3 in southern mid-latitudes.

Observations of CFCs allow us to examine the accuracy of the model simulation of the dynamical contribution to seasonal variations in CH_3CCl_3. Unfortunately, observations of CFC-11 and CFC-12 from Palmer Station proved unsuitable for the present analysis because of marked step changes up to 6 and 8 ppt, respectively, in the records [*Cronn et al.*, 1986], attributable to replacement of secondary standards (recalibration). (Smaller step changes, up to 2 ppt, might have slightly affected the apparent amplitude of seasonal variations in CH_3CCl_3 at Palmer Station shown in Figure 14*b*.) As we will see below, problems associated with recalibration affect the ALE data also.

There are six sets of measurements of CFCs from Tasmania obtained using two instruments, HP-5840 and HP-5880, and, in the case of CFC-11, using two different columns, silicone (S) and porosil (P), for each instrument. The 5840 data for CFC-11 from Tasmania, both S and P, do not show significant seasonal variations, as follows from correlograms in Figure 12*b*. The 5880 (P) measurements of CFC-11 and the 5840 and 5880 measurements of CFC-12 exhibit small seasonal variations similar to those predicted by the model, as shown in Figure 15. (See also correlograms for these observations in Figures 12*b* and 12*c*).

The remaining observations for CFCs at Tasmania, 5880 S measurements of CFC-11, were shown by *Fraser et al.* [1985*a*] to display an annual cycle that appeared to be similar in amplitude and phase to the annual cycle in CH_3CCl_3. They pointed out that these data might present evidence against the suggested dominant role of chemistry in determining seasonal variations of CH_3CCl_3.

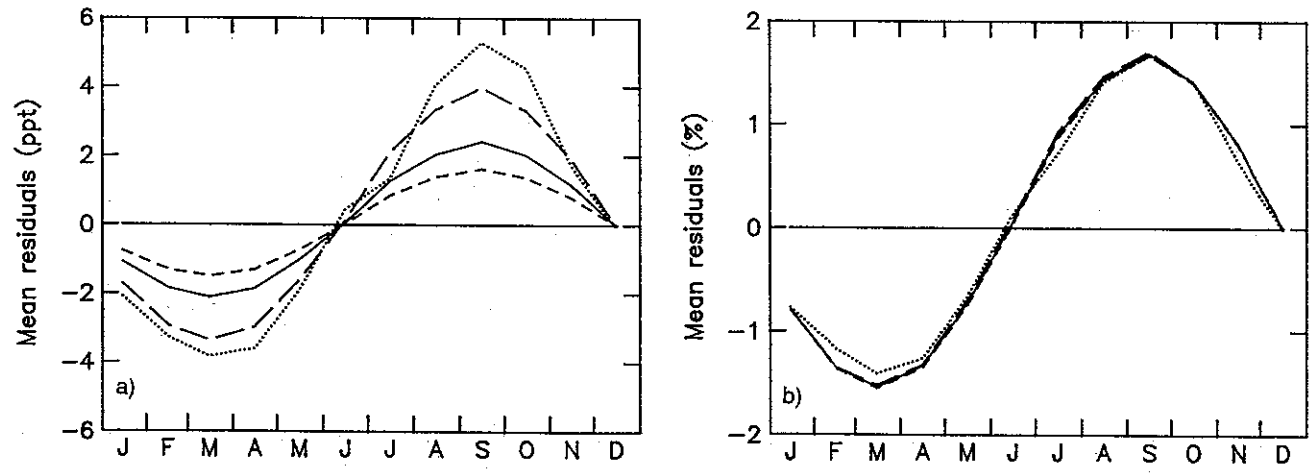

Fig. 13. Seasonal variations in concentration *(a)* $c(t)$ and in *(b)* $[c(t) - c_{trend}(t)]/c_{trend}(t)$ for different levels of emissions and absolute calibration. Concentration $c(t)$ satisfies (5) of section 4.2 with the initial condition $c(0)$=75 ppt and with a lifetime L expressed as $k_o^{-1}\cdot[1+\cos(\omega\cdot t)]^{-1}$, where $k_o = 0.1\ y^{-1}$ (an annual mean rate of loss) and $\omega = 2\pi\ y^{-1}$. The term $p(t)$ of (5) here represents a sum of the flux divergence and the source term. The baseline concentration $c_{trend}(t)$ satisfies the (5) for $L = k_o^{-1}$. Solid, short- and long-dashed lines correspond to F_p/F_c equal, respectively, to 1, 0.5 and 2. For all three cases, $p(t)$ is assumed equal to annual emissions of CH_3CCl_3 as in Table B2 for 1978-1986. Dotted lines represent the case of $F_p/F_c = 1$ and $p(t)$ increasing by 30% per year from the 1978 level. The annual cycle was averaged over 9 years. Note that amplitudes A_{rel} (in percent) are virtually the same for these four cases, while associated amplitudes A_{abs} (in pptv) vary by more than a factor of 7.

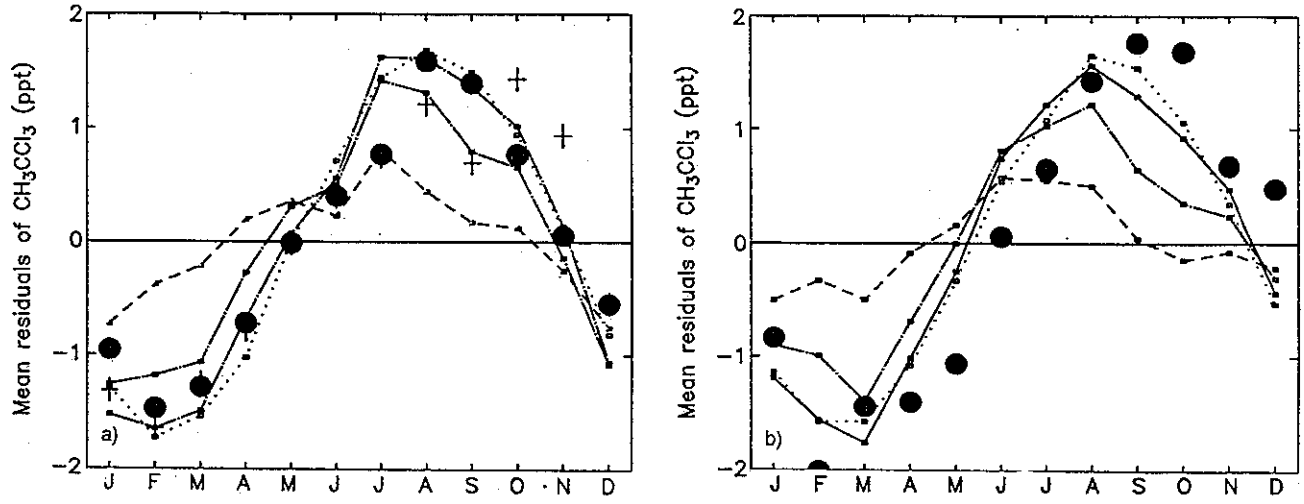

Fig. 14. Annual cycle of CH_3CCl_3 in southern mid-latitudes at Tasmania (*a*) [*Fraser et al.*, 1985*a*, *b*, 1987] and at Palmer station (*b*) [*Cronn et al.*, 1986]. Circles and crosses denote observations with the 5880 and 5840 instruments, respectively. Continuous curves correspond to simulations of MCL/OH (solid lines), MCL/ASEAS (dashed lines), and MCL/50%OH (dot-dashed lines) for the grid box containing the observational site, at the surface. The three simulations differ in the way the loss frequency of CH_3CCl_3 is calculated: for MCL/OH it is based on the standard OH, for MCL/50%OH the standard OH field was multiplied by 0.5, whereas for MCL/ASEAS the loss rate is assumed constant throughout a year and in each grid box is equal to the annual mean value calculated for this box in the MCL/OH simulation. Dotted lines represent computed zonal means for the latitudinal bands containing the sites, for MCL/OH.

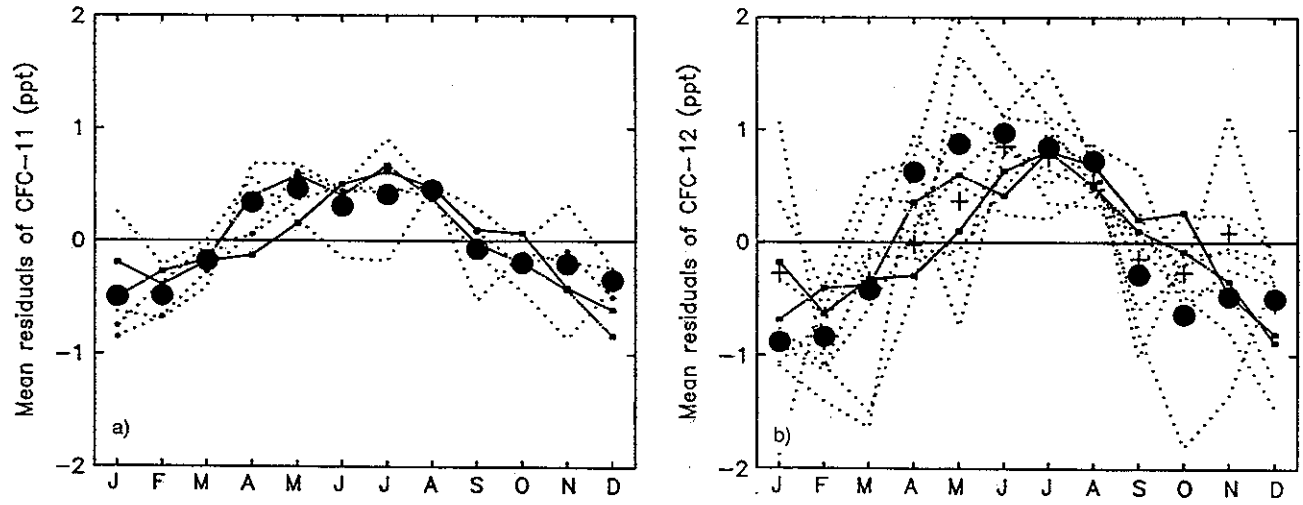

Fig. 15. Annual cycles of (*a*) CFC-11 and (*b*) CFC-12 at Tasmania. Circles and crosses correspond to observations with the 5880 (P) and 5840 instruments, respectively [*Fraser et al.*, 1985*a*, *b*, 1987]. Dotted lines denote observations for individual years. Solid and dot-dashed lines represent the annual cycle calculated for Tasmania at the surface, in the simulations with the FSD and SSD, respectively.

However, we believe that the annual cycle of CFC-11 derived from the 5880 S data is an artifact of recalibration. In 2 out of 3 years of the record, recalibration was associated with an apparent change of more than 2 ppt, in the same direction at a given season (April-May 1982, an increase of about 4 ppt; March-April 1984, an increase of about 3 ppt), as shown in Figure 16*a*. There was a compensating decrease of 2.5 ppt in the opposite season (November-December 1984). These step changes introduced systematic errors in the annual cycle derived for CFC-11, artificially exaggerating the amplitude of seasonal variations. Figure 16*b* shows the "annual cycle" of CFC-11 derived from the 5880 S data for the period Jan. 1982-Dec. 1984 (triangles) as compared to the "annual cycle" derived for a longer record Jan. 1982-Dec. 1985 (asterisks). The addition of the 1985 data to the record (not available for the analysis by *Fraser et al.* [1985*a*]) reduced the amplitude of the apparent annual cycle. If we exclude the 1982 data, eliminating the impact of the recalibration in April 1982, the amplitude is further reduced (diamonds), bringing it closer to that displayed by the 5880 P data (Figure 15*a*). Some effect of recalibration is discernible for CFC-12 in a few cases. Because of the schedule adopted for exchanges of standards, these inhomogeneities tend to enhance the inferred seasonal variations.

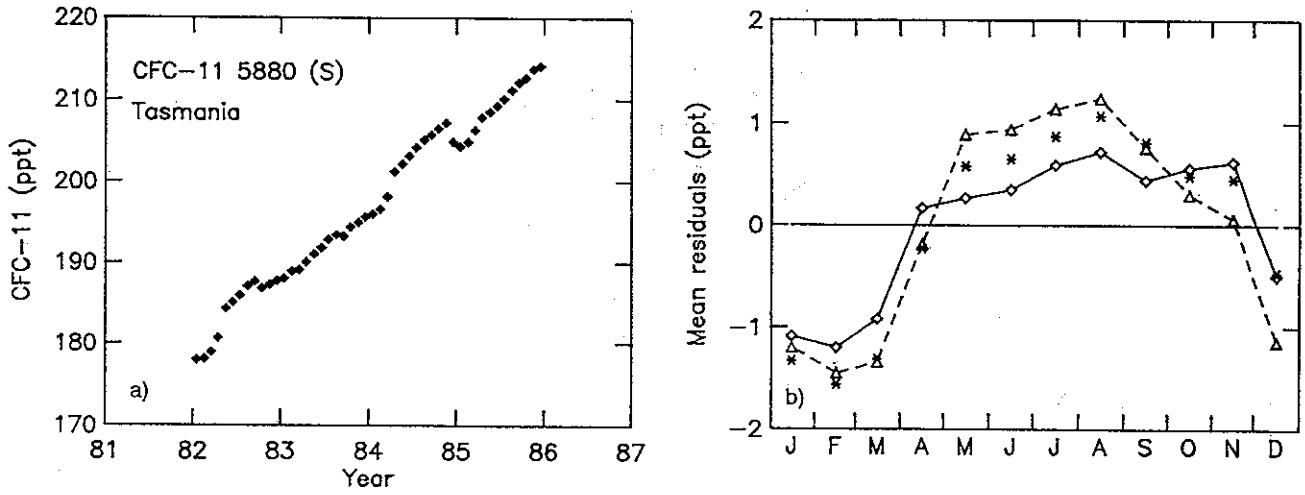

Fig. 16. Observations of CFC-11 with the 5880 instrument (S) [*Fraser et al.*, 1985*a*, *b*, 1987]. Note in (*a*) the step-changes in April-May of 1982, March-April and November-December of 1984. (*b*) The "annual cycle" derived for the periods: Jan. 1982-Dec. 1984 (triangles connected by a dashed line), Jan. 1982-Dec. 1984 (asterisks), and Jan. 1983-Dec. 1985 (diamonds connected by a solid line).

To summarize our analysis of CFC observations at Tasmania, we conclude that most of the 5840 data do not exhibit a significant annual cycle, consistent with *Fraser et al.* [1985*a*]. In contrast to these, the 5880 data display significant annual cycles, which are reproduced by the model. The 5840 instrument has a lower signal-to-noise ratio and may therefore fail to detect small seasonal variations [cf. *Fraser et al.*, 1985*a*]. However, it is conceivable that the derived annual cycles of CFCs at Tasmania could be artificially enhanced by recalibration. We conclude that existing data define an upper limit for possible seasonal variations in CFCs at southern mid-latitudes. The model is either accurate in simulating the annual cycle of CFCs or it coincidentally reproduces the magnitude and phase of an artifact. In any case the model does not underestimate the amplitude of seasonal variations in CFCs as defined by available observations. The same conclusion should apply to the dynamical component of the seasonal variations of CH_3CCl_3.

Prather [1985, 1988] estimated seasonal variations in emission rates for various halocarbons using ALE data collected during pollution episodes at Adrigole. He assumed that emission rates for CFC-11 are uniform with season, based on the diverse uses of this compound. Seasonal patterns for enhancements of concentrations of CFC-12 and CH_3CCl_3, relative to that of CFC-11, were identified and attributed to seasonal variations in emission rates. The annual modulation of CH_3CCl_3 release was found to be less than 20%, with maximum release in spring, minimum in summer. Seasonal changes in emission rates of this magnitude have no effect on computed annual cycles in the southern hemisphere, and a small effect in the northern hemisphere, as shown in section 6.2.2.

Our analysis suggests that computed fields for global OH can be tested by comparing observed and computed seasonal variations in CH_3CCl_3 at southern mid-latitudes, where the annual cycle of CH_3CCl_3 is determined by seasonal variations in the loss rate. Figure 17 shows data for CH_3CCl_3 from Figure 14, except that the monthly residuals have been divided by c_{trend} prior to averaging. The solid, dot-dashed, and dashed lines correspond to the simulations MCL/OH, MCL/50%OH, and MCL/ASEAS, respectively. Differences between the MCL/OH or MCL/50%OH and MCL/ASEAS reflect the influence of chemistry. Simulations with standard OH and with OH reduced by 50% provide an upper and lower limit, respectively, for the amplitude A_{rel} of seasonal variations observed at Tasmania (Figure 17*a*). To a good approximation, this amplitude varies linearly with OH, as may be seen by comparing the curve for MCL/50%OH with curves for MCL/OH and MCL/ASEAS. (Note that this is not the case for the amplitude A_{abs} of variations shown for the absolute concentrations in Figure 14.) The results in Figure 17*a* imply that, if a single scaling factor is used to calibrate the global OH field, computed concentrations should be multiplied by a factor 0.75 ± 0.25, and factors outside this range would be inconsistent with observed seasonal variations. If we assumed that the model overestimates the dynamical contribution to seasonal variations at Tasmania, as might be concluded from the 5840 data for CFCs, then the best value for the scaling factor would be closer to 1.

The data from Palmer station (Figure 17*b*) suggest a larger amplitude for seasonal variations in CH_3CCl_3 than at Tasmania and slightly greater than computed with the standard OH. However, we place greater confidence on the estimate derived from observations at Tasmania because of possible problems with recalibration at Palmer and the longer data record at Tasmania. (The annual cycle at Palmer was derived using 3 years of data, omitting the first 7 and last 5 months of the record to avoid the influence of the two large step-changes.)

Thus far we used a single scaling factor to calibrate the global OH field with respect to seasonal variations in CH_3CCl_3 observed at Tasmania and Palmer station. Now we will use the model to define the spatial extent of the OH field that determines the annual cycle of CH_3CCl_3 at southern mid- and high- latitudes. Figures 18*a* and 18*b* show seasonal variations computed for CH_3CCl_3 using loss rates based on standard OH at specified latitudes with aseasonal (like in MCL/ASEAS) loss frequencies imposed elsewhere. If temporal variations in the loss rate are confined to the latitude zone at 44±4°S (short-long-dashed lines), the amplitude of the annual cycle in the southern hemisphere is increased only slightly over the amplitude for MCL/ASEAS (computed using aseasonal loss rates everywhere and denoted by short-dashed lines). Annual cycles are enhanced as seasonal variations in the loss rate are extended northward; about 75% of the seasonal signal at southern mid-latitudes is obtained when the model includes temporal variations of OH from 90°S to about 25°S. Further in-

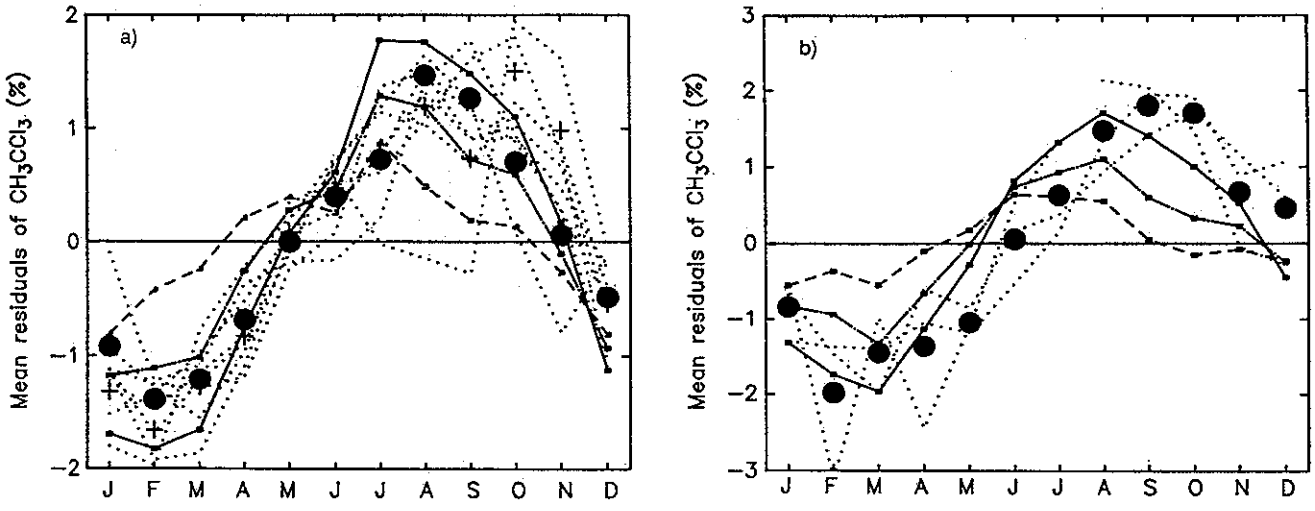

Fig. 17. Annual cycle in $[c(t) - c_{trend}]/c_{trend}$ for CH_3CCl_3 in southern mid-latitudes at Tasmania (*a*) and at Palmer station (*b*). Circles and crosses correspond to the mean annual cycle derived from observations with the 5880 and 5840 instruments, respectively [*Fraser et al.*, 1985*a*, *b*, 1987; *Cronn et al.*, 1986]. Dotted lines represent individual years of observations. Solid, dashed, and dot-dashed lines show the annual cycle derived from the simulations MCL/OH, MCL/ASEAS and MCL/50%OH, respectively (see Fig. 14 for the definition of these simulations). The simulations are shown for SSD. Note that the MCL/50%OH curve is almost equidistant from the MCL/OH and MCL/ASEAS curves. This is not the case for the variations in concentration shown in Fig. 14, where the decrease in amplitude caused by reduction in the loss rate was offset by accelerated growth of concentration associated with the lower loss rate. Also note a change between Figures 14 and 17 in disposition of observations versus the MCL/OH simulation, reflecting the fact that simulated concentrations for standard OH (MCL/OH) are slightly lower than those observed (see Fig. 4).

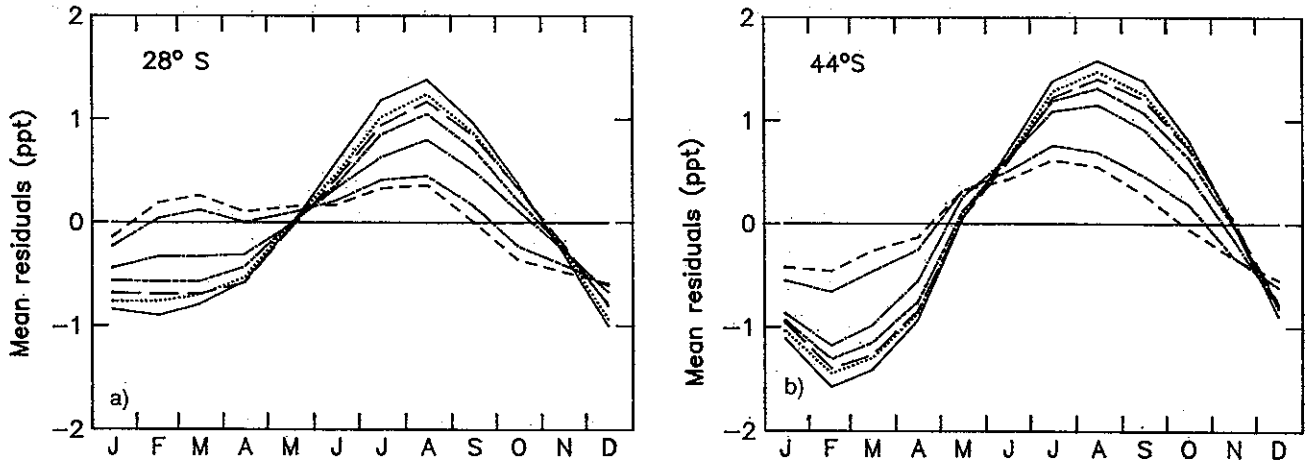

Fig. 18. Spatial extent of the impact of seasonal variations in the loss rate on the annual cycle in CH_3CCl_3. Panels (*a*) and (*b*) show seasonal variations of CH_3CCl_3 at 28°S and 44°S, respectively, computed using aseasonal loss frequencies at specified latitudes and those based on standard OH assumed elsewhere. Solid and short-dashed lines represent limiting cases of the MCL/OH and MCL/ASEAS simulations, respectively. The intermediate lines, in the order of decreasing amplitude, correspond to the simulations with aseasonal loss rate assumed: (1) north of 24°N (dotted lines); (2) north of 16°S (long-dashed lines); (3) north of 24°S (chain-dashed lines); (4) north of 32°S (dot-dashed lines); (5) everywhere outside the zone 44°S ± 4° (short-long-dashed lines). Panels (*c*) and (*d*) show seasonal variations in OH and in the chemical component of CH_3CCl_3 (defined as difference between MCL/OH and MCL/ASEAS), respectively, at the surface for various latitudes: 20°S (chain-dashed line), 28°S (dot-dashed line), 44°S (solid line) and 76°S (dashed line). Zonally and annually averaged OH concentrations (in 10^5mol cm^{-3}) for 20°S, 28°S, 44°S, and 76°S are, respectively, 10.0, 8.6, 2.75, and 0.4. Two additional curves in panel (*d*) show variations at 12°S and 4°S (long-dashed and dotted line, respectively). Panel (*e*) shows the chemical component of seasonal variations in CH_3CCl_3 at 44°S for various pressure levels: ~920 mbar (solid line), ~650 mbar (chain-dashed line), ~480 mbar (long-dashed line), ~325 mbar (short-dashed line), and ~200 mbar (dotted line).

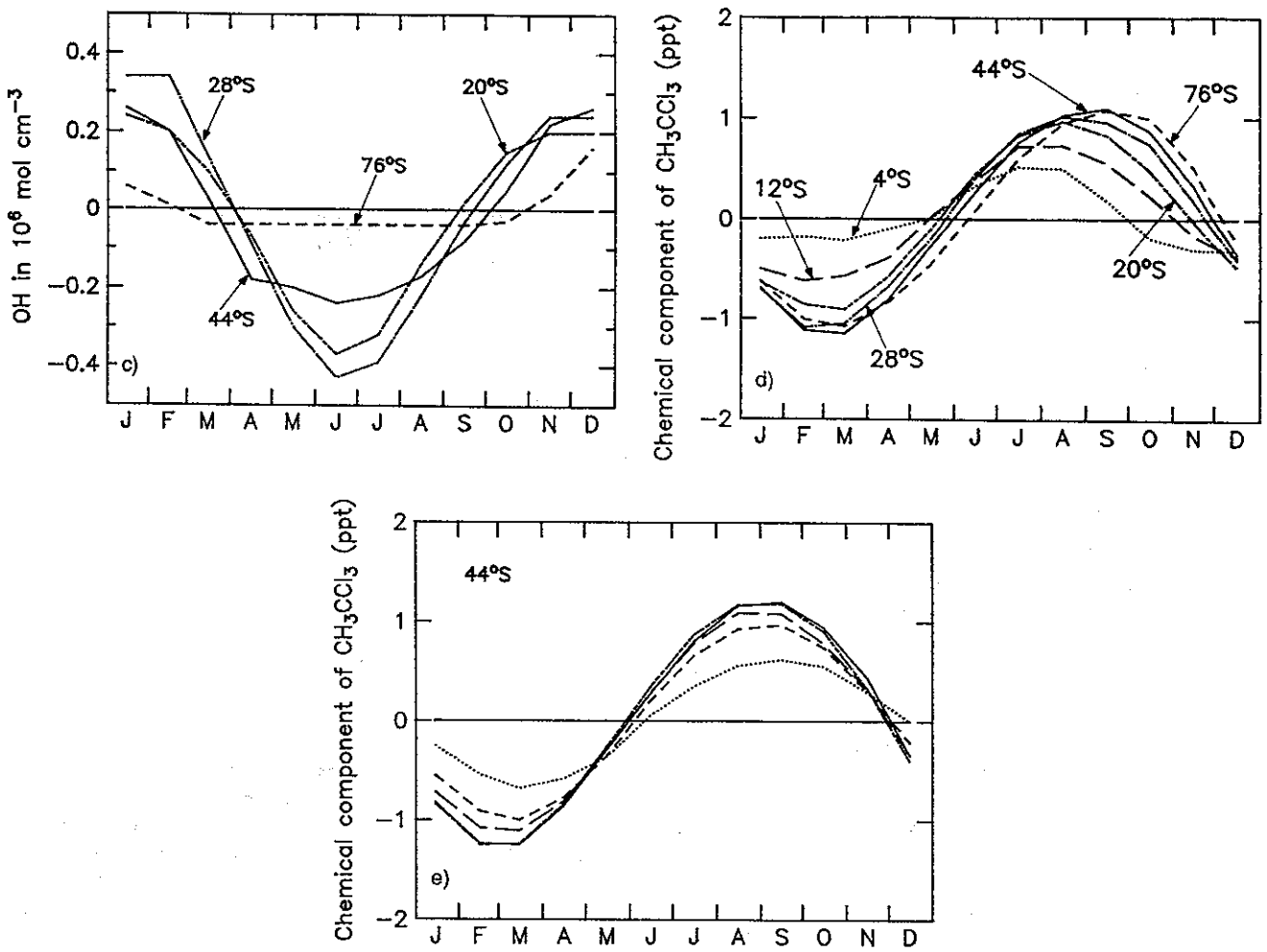

Fig. 18. (continued)

creases in the seasonal amplitude are realized as temporal variations are extended to the tropics. A small part (~10%) of the chemical signal appears to reflect OH variations in the northern hemisphere.

On the seasonal time scale the distribution of CH_3CCl_3 south of about 25°S appears to behave as a coherent entity, with seasonal variations of CH_3CCl_3 at 28°S being similar to those at 44°S, irrespective of the latitudes for which temporal variations of OH are included in the model. Although the amplitudes for seasonal variations in OH at various latitudes from 20°S to the South Pole (Figure 18*c*) differ by more than a factor of 10, the influence of chemistry on the annual cycle of CH_3CCl_3, expressed as the difference between the two simulations, MCL/OH and MCL/ASEAS, depends little on latitude (Figure 18*d*). The annual cycle in the chemical component is virtually constant from the surface up to 400 mbar (Figure 18*e*). These results indicate that annual cycles of CH_3CCl_3 at Tasmania provide a test of the OH concentration averaged over most of the southern hemisphere, weighted by frequency of reaction with CH_3CCl_3.

6.2.2. *Northern mid-latitudes.* The model reproduces the annual cycle of CH_3CCl_3 observed at Oregon [*Prinn et al.*, 1987], as shown in Figure 19. The solid and dashed lines correspond to the simulations with standard OH (MCL/OH) and with aseasonal loss (MCL/ASEAS), respectively, and the chain-dashed line, to the simulation with standard OH and with emissions varying by season as discussed by *Prather* [1988]. The annual cycle exhibits a sharp minimum in summer. The observed peak-to-peak variation is about 8 ppt, as compared to ~11 ppt for MCL/OH, and about 6.5 ppt for aseasonal loss. There is evidently a strong dynamical component to the annual cycle. The observed annual cycle for CFC-11 (Figure 20) is also similar to model results and to the annual cycle of MCL/ASEAS. Unfortunately, only short records are available for CFCs (2 and 3 full years for CFC-12 and CFC-11, respectively), and we cannot accurately define observed mean annual cycles associated with dynamics alone at this station.

As discussed in section 5, computed concentrations at Adrigole are strongly affected by a nearby source region. Monthly medians, used as a surrogate for simulated background concentrations at Adrigole, display an annual cycle dominated by elevated concentrations in different months for different years of the GCM simulation (e.g., May for FSD and March for SSD), indicating the large influence of transient events. Annual cycles for grid boxes directly to the west and southwest of Adrigole show more regular seasonal variations. The grid box southwest of Adrigole (designated below as SWoA) appears to be least affected by the "local contamination." We shall compare annual cycles in this box to the

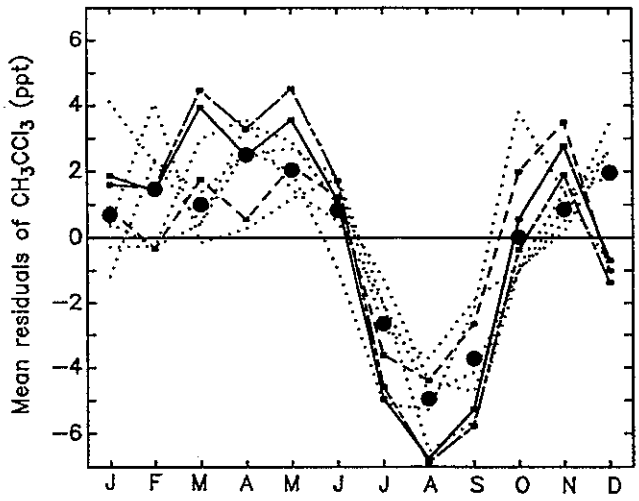

Fig. 19. Annual cycle of CH_3CCl_3 at Oregon. Observations [*Prinn et al.*, 1987] are designated by circles for mean variations and dotted lines for variations in individual years. Solid and dashed lines correspond to MCL/OH and MCL/ASEAS, respectively. The chain-dashed line represents the simulation with the emissions of CH_3CCl_3 assumed to vary with season (as in *Prather* [1985,1988]) and with the loss rate based on standard OH. The simulations are shown for SSD.

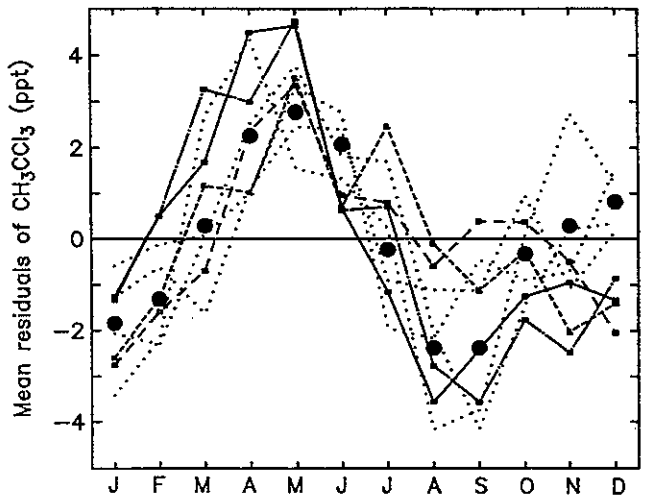

Fig. 21. Annual cycle of CH_3CCl_3 for the grid box directly southwest of the Adrigole box. The solid and dot-dashed line correspond to the MCL/OH simulations with the FSD and SSD, respectively. Long- and short-dashed lines represent the MCL/ASEAS simulations for FSD and SSD, respectively. Observed concentrations at Adrigole [*Prinn et al.*, 1987] are denoted by circles for the mean annual cycle and by dotted lines for the individual years.

"unpolluted" Adrigole data reported by the ALE investigators. Figure 21 shows computed annual cycles for CH_3CCl_3 in the box SWoA for MCL/OH and MCL/ASEAS. Both simulations display a maximum in spring and a minimum in late summer, indicating a significant dynamical contribution to the annual cycle. Model results for the SWoA box reproduce major features of the annual cycle in CH_3CCl_3 observed at Adrigole.

6.2.3. *Tropics.* The variations of halocarbons observed at Barbados (13°N, 59°W) [*Prinn et al.*, 1987; *Cunnold et al.*, 1986] do not allow an easy interpretation. Monthly variances of CH_3CCl_3 throughout the record are larger than those for CFCs, indicating noisy data. These variances for CH_3CCl_3 at Barbados are as large as those at Adrigole, a site known to be affected by the adjacent source region. Observations of CH_3CCl_3 exhibit an annual cycle with a pronounced minimum in fall (Figure 22), but CFCs do not display a significant annual cycle, as shown by correlograms in Figure 12*f*. The model predicts significant seasonal variations, controlled by dynamics, for both CH_3CCl_3 and CFCs. Model results show a minimum in fall, consistent with observations of CH_3CCl_3, but a spring maximum is predicted that is not observed. Possible explanations of the apparent inconsistencies include: seasonal change in the emission rates specific for a given tracer in a nearby source region; a geographic distribution of sources for CH_3CCl_3 different from CFCs in adjacent regions; and difficulties

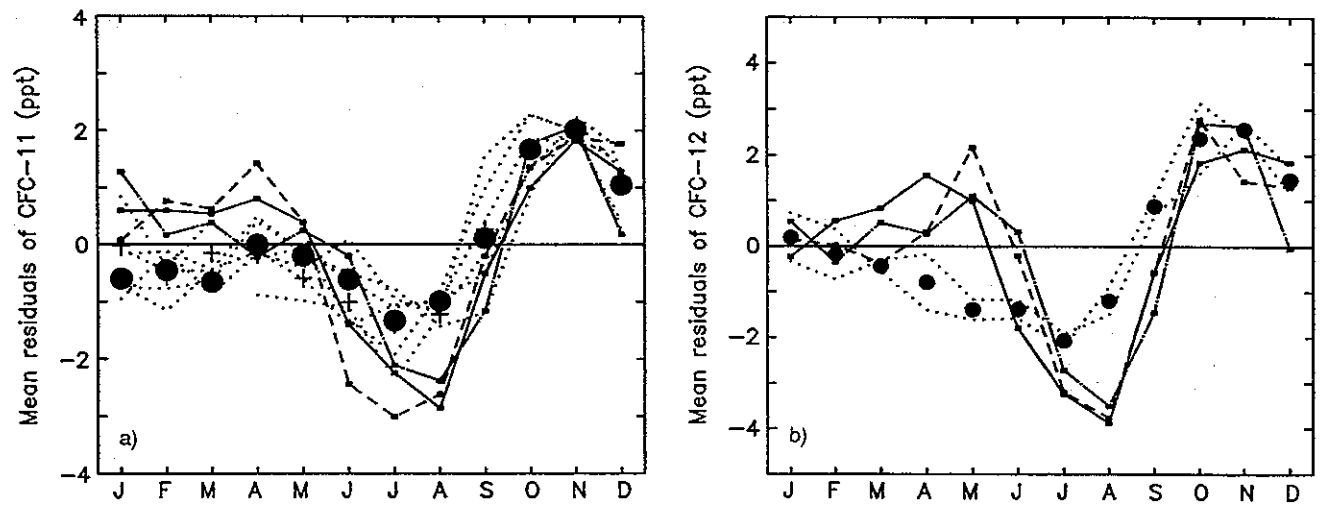

Fig. 20. Annual cycles at Oregon for (*a*) CFC-11 and (*b*) CFC-12 (solid and dot-dashed lines for FSD and SSD, respectively). Observations [*Cunnold et al.*, 1986] are represented by large circles and crosses for the porosil and silicone columns, respectively. Individual years of observations are denoted by dotted lines. (Short-dashed lines represent annual cycles computed (with SSD) for the model box west of the Oregon box.

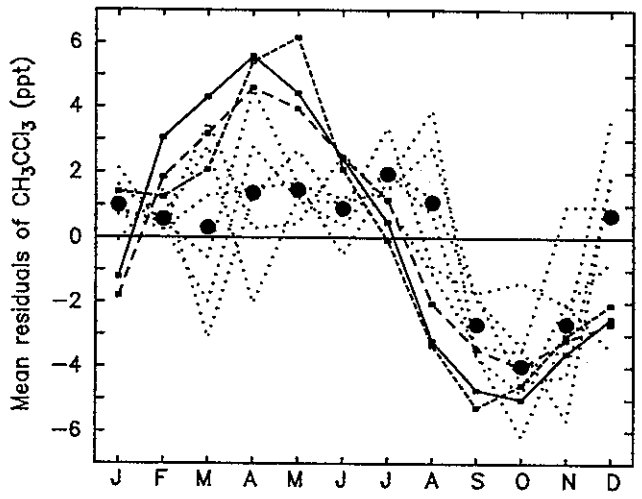

Fig. 22. Annual cycle of CH_3CCl_3 at Barbados. Observations [*Prinn et al.*, 1987] are represented by circles for the mean variations and by dotted lines for individual years of the record. The solid line corresponds to the simulation MCL/OH for the FSD. The long- and short- dashed lines represent the MCL/ASEAS simulations for FSD and SSD, respectively.

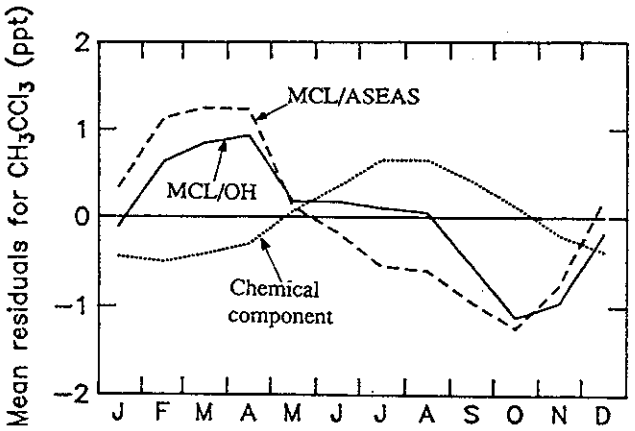

Fig. 24. Annual cycle of CH_3CCl_3 simulated for Samoa (solid line). The dashed line corresponds to the MCL/ASEAS simulation. The dotted line represents the chemical component, defined as a difference between the MCL/OH and MCL/ASEAS simulations.

with model simulation of transport in this region. The large variances in monthly means of CH_3CCl_3, not observed for CFCs, could indicate problems with data quality.

Observed variations at Samoa (12°S, 171°W) appear to be significant at the 95% confidence level for CFC-11 (P) and CFC-12, and marginally detectable for CFC-11 (S) as shown in Figure 12*g*. Observed concentrations of CFCs are higher in January–April than in July–October, consistent with model results, as shown in Figure 23. For CH_3CCl_3 the model predicts that chemical and dynamical components of seasonal variations should be out of phase (Figure 24), resulting in small net variations (about 1 ppt); the observed annual cycle of CH_3CCl_3 appears to be insignificant (Figure 12g). Model results are not inconsistent therefore with the observed seasonal behavior of halocarbons at Samoa.

6.3 *Processes Regulating Annual Cycles of Halocarbons*

As shown in section 6.2, most of the observed seasonal variations in CFCs and CH_3CCl_3 can be reproduced assuming constant emissions throughout a year. Transport processes determine annual cycles for CFCs at all latitudes, and strongly influence annual cycles of CH_3CCl_3 in the northern hemisphere and in the southern tropics. The chemistry of OH determines seasonal variations of CH_3CCl_3 only for southern middle and high latitudes, even though the absolute amplitude (e.g., in pptv) of the annual cycle for

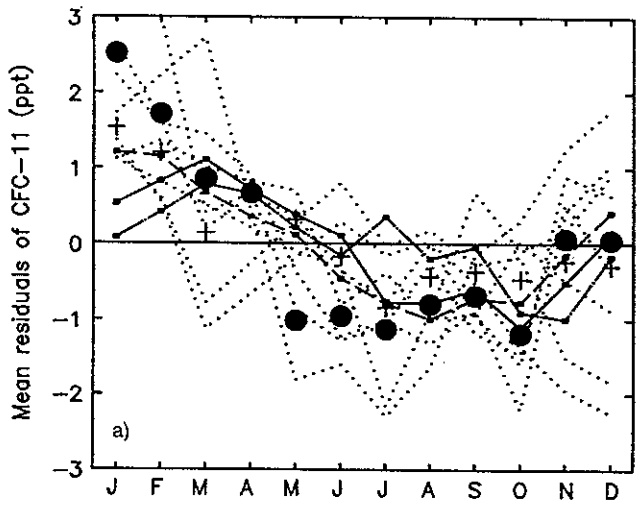

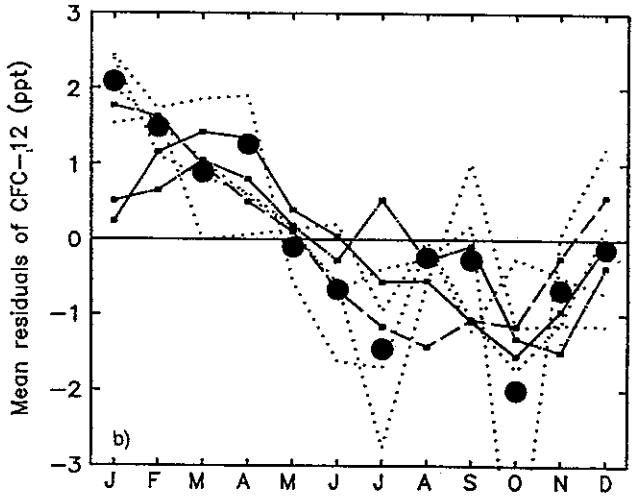

Fig. 23. Annual cycle of (*a*) CFC-11 and (*b*) CFC-12 at Samoa. Observations [*Cunnold et al.*, 1987] are represented by circles and crosses for the porosil and silicone columns, respectively. Dotted lines denote variations for individual years of observations. Solid and dot-dashed lines correspond to the simulations for the grid box, containing Samoa at the surface, computed with the FSD and SSD, respectively. Dashed lines show an annual cycle simulated for the grid box with the center located 26.5° west of Samoa (FSD).

CH_3CCl_3 attributed to chemistry is twice as high for northern mid-latitudes as for southern mid-latitudes (Figure 25), reflecting both higher concentrations of CH_3CCl_3 and higher concentrations of OH in the north. Concentrations of OH in summer are higher in the north mainly due to higher concentrations of NO_t and O_3 and to larger areas of land (higher surface albedo).

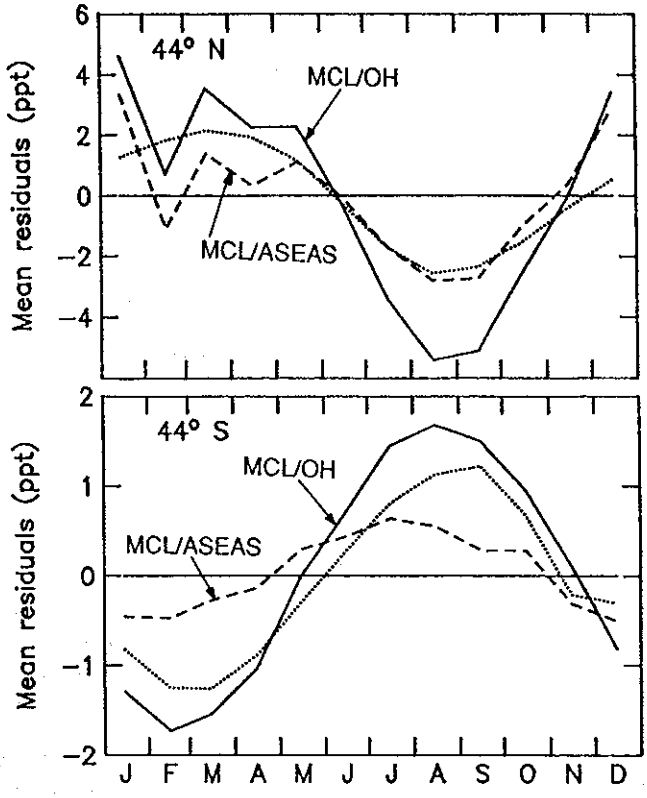

Fig. 25. Annual cycles for a zonal mean at 44°N and 44°S. Solid and dashed lines represent MCL/OH and MCL/ASEAS simulations, respectively. Dotted lines correspond to the chemical component in the variations defined as a difference between MCL/OH and MCL/ASEAS.

The annual cycles predicted for CFCs or MCL/ASEAS at northern mid-latitudes vary markedly with longitude, both in amplitude and phase (Figure 26*a*). Near source regions during summer, ventilation of the continental boundary layer by convection is more vigorous than in other seasons and concentrations at the surface are lowest [*Prather et al.* 1987]. The annual cycle has opposite phase aloft, as shown in Figure 27 for grid boxes containing Michigan and Germany.

At Oregon and SWoA the computed annual cycle has a semiannual component (also discernible in the observations, as shown in Figures 19–21, and 12*d* and 12*e*) with minima in winter and summer. These stations lie in the path of westerlies carrying marine air with relatively low concentrations of halocarbons. In winter, when westerlies are stronger, concentrations at these locations decrease, in conjunction with an increase in concentrations at sites downwind of major source regions, e.g., at Alaska [*Prather et al.* 1987; *Khalil and Rasmussen*, 1983]. The summer minimum at Oregon and SWoA reflects the seasonal enhancement of convective mixing over the continents. This effect is partly offset at SWoA by intensified transport of air from Europe to the Atlantic in summer (compare concentration contours in Figure 7 for January and July).

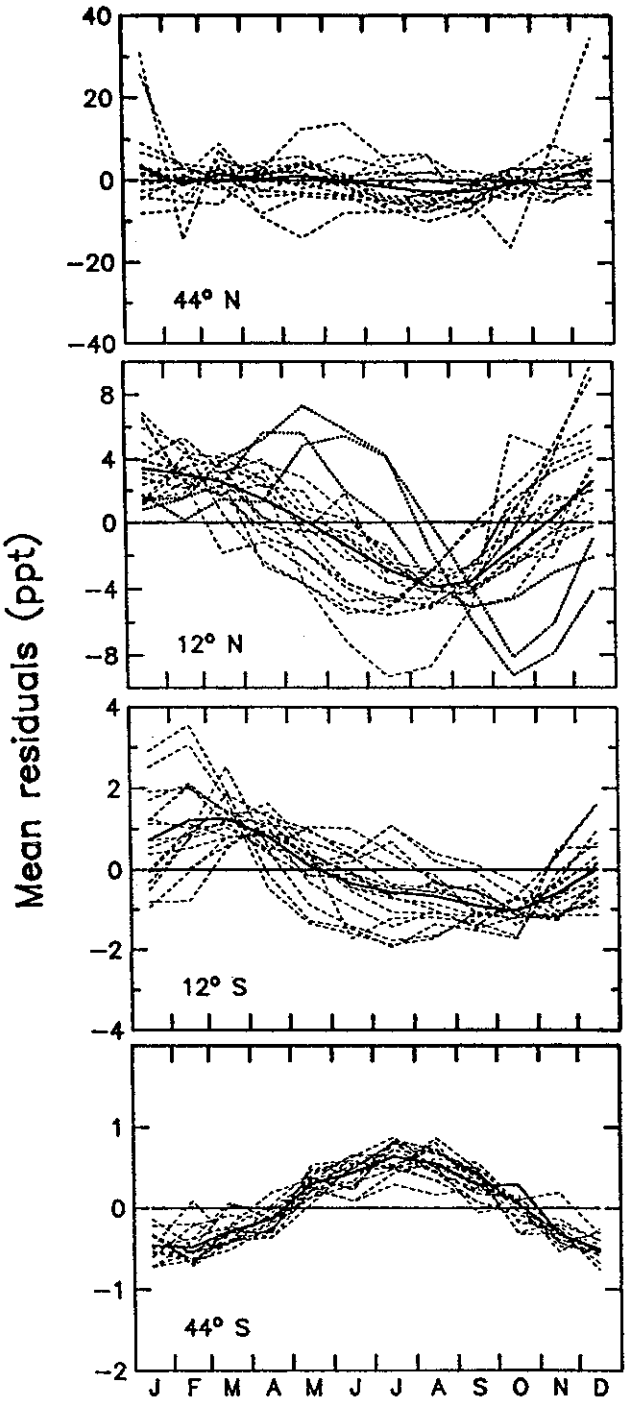

Fig. 26. Annual cycles at the surface along model zones 8° wide centered at 44°N, 12°N, 12°S, and 44°S for MCL/ASEAS, given with a 20° step in longitude (dashed lines). Solid lines represent annual cycles for zonally averaged concentrations. Dotted lines for 12°N correspond to the grid boxes over the Atlantic. Variations for each grid box are given with respect to the base line characteristic of this box, and the annual cycle for the zonal mean represents variations with respect to the c_{trend} for zonally averaged concentrations.

Longitudinal variations in concentration and in the associated annual cycle decrease with distance from source regions, as seen in Figures 7 and 26. The annual cycles for the northern tropics at the surface are similar around the model zone, with the exception of the Atlantic. Annual cycles in the southern hemisphere show little zonal asymmetry.

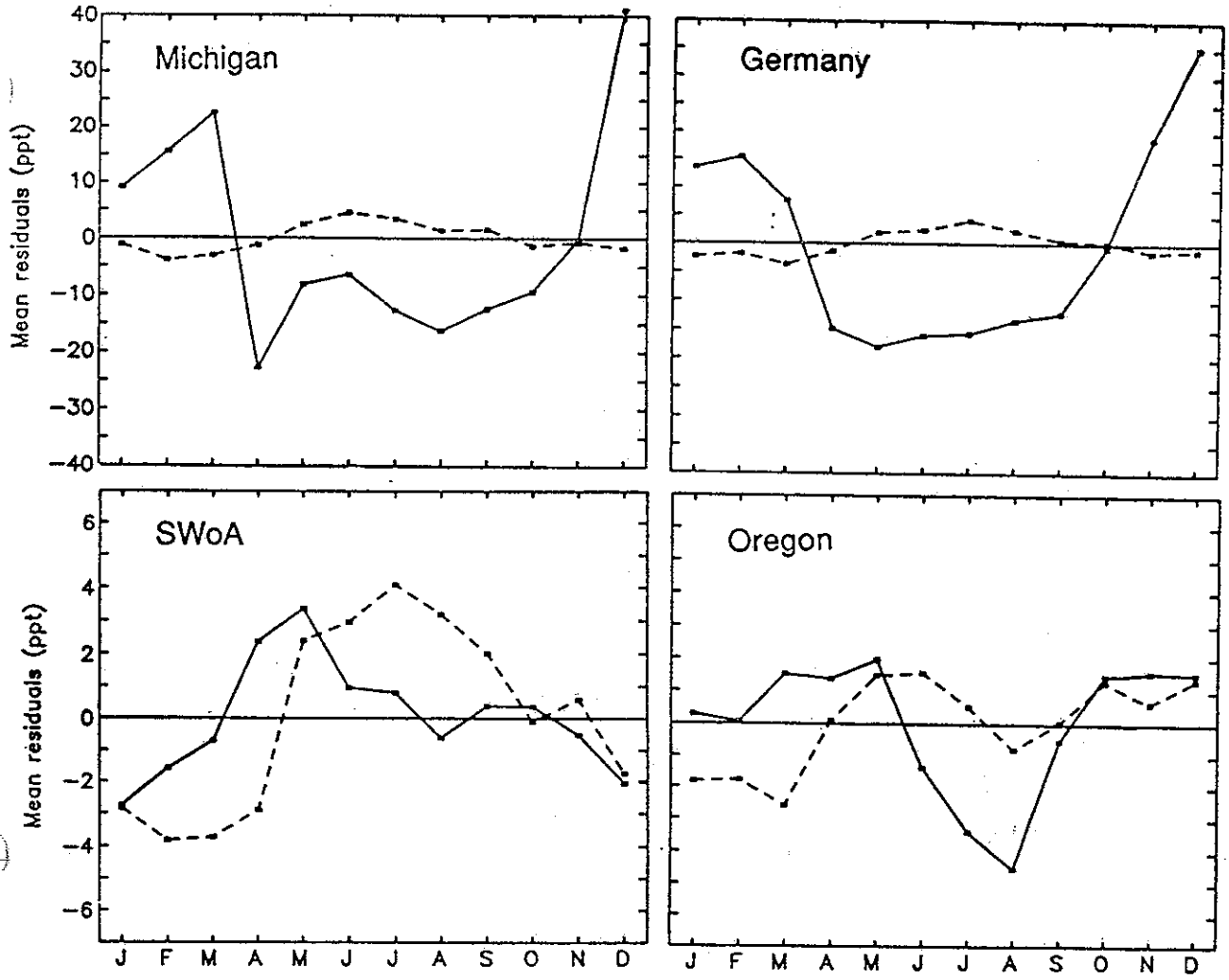

Fig. 27. Annual cycles of MCL/ASEAS at various longitudes at 44°N: Michigan, Germany, Oregon and the Atlantic directly southwest of Adrigole. Solid and dashed lines represent concentrations at the surface and at 500 mbar, respectively.

The basic patterns of global dispersion of long-lived tracers emitted at the surface in northern mid-latitudes are illustrated in Figure 28, where zonally averaged fluxes for MCL/ASEAS are represented by arrows for each σ layer. Tracers are carried towards the equator in the lower troposphere within the northern tropical cell. They are lifted to the upper troposphere in the zone of tropical convergence, whence they are moved southward and downward in the southern tropical cell [cf. *Plumb and Mahlman*, 1987].

The role of various transport processes in regulating annual cycles in the tropics is illustrated in Figure 29, for the two lowest σ levels in zones 8° wide centered at 12°N and 12°S. The solid line represents the net rate of change in tracer mass in the zone, with the annual mean marked by a dotted line. The net change is a sum of the divergence of advective and diffusive fluxes (long-dashed line), change by convection (dot-dashed line), and two components (emissions and loss) assumed constant throughout the year (not shown). We also show (short-dashed line) the divergence of the flux associated with zonal mean velocities computed every 8 hours, denoted as mean flow. Periods when the net rate of change is greater than the annual mean (e.g., September-December for 12°N and October-February for 12°S) correspond to periods when the zonally averaged concentrations are increasing relative to the annual mean (see Figure 26).

Enhancement of the Hadley-type circulation in northern winter contributes to the increase of concentration for that season in the northern tropics, but, during southern winter, stronger circulation leads to lower concentrations in the southern tropics. The difference can be explained by the opposite roles played by the two tropical cells in delivering tracers to the northern and southern tropics. The northern tropical cell transports industrial gases from mid-latitude source regions to the tropics, while the southern cell ventilates the tropics by bringing air northward that is relatively depleted in tracers. Tracers are delivered to the low troposphere of the southern tropics by convection from aloft. The migration of the ITCZ toward the summer hemisphere is expected to amplify the effect of seasonal fluctuations in the strength of the tropical cells, contributing to the increase of concentration in the southern tropics in summer, and at the low latitudes of northern tropics (south of the northern limit of the ITCZ) in winter. Determination of the exact role of the migration of the ITCZ would involve additional simulations, in particular, studies with sources placed in the tropics.

In the lower troposphere at southern mid-latitudes, convection brings tracer from aloft, providing the dominant positive contribution to the net change in tracer concentration (Figure 29*c*). In December–February, when the region falls in the direct path of the descending branch of the southern tropical cell, advection from the

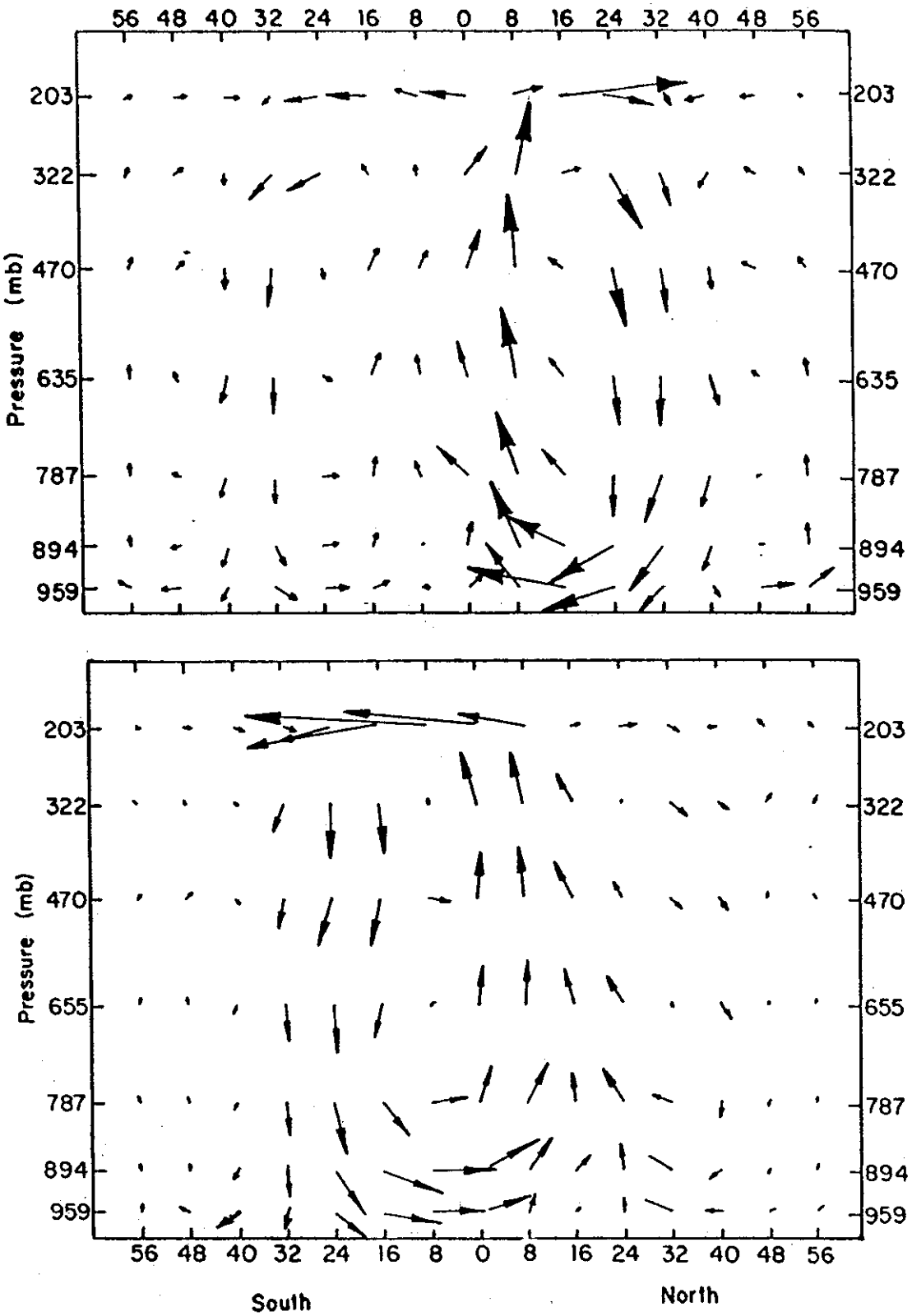

Fig. 28. Zonally averaged net fluxes (including advection, diffusion and convection) in the simulation of MCL/ASEAS for January and July, upper and lower panel, respectively . The length and direction of arrows reflects the magnitude and direction of meridional and vertical fluxes. Fluxes in the CTM are defined at the boundaries of the grid boxes. Height is resolved in σ coordinates; vertical layers, chosen here to represent the vertical grid, correspond to the uniform surface pressure of 984 mbar. The arrows are shown at the boundaries of latitudinal bands, in the middle of vertical layers; the vertical component represents a mean of the two vertical fluxes through the top of the layer for adjacent latitudinal bands.

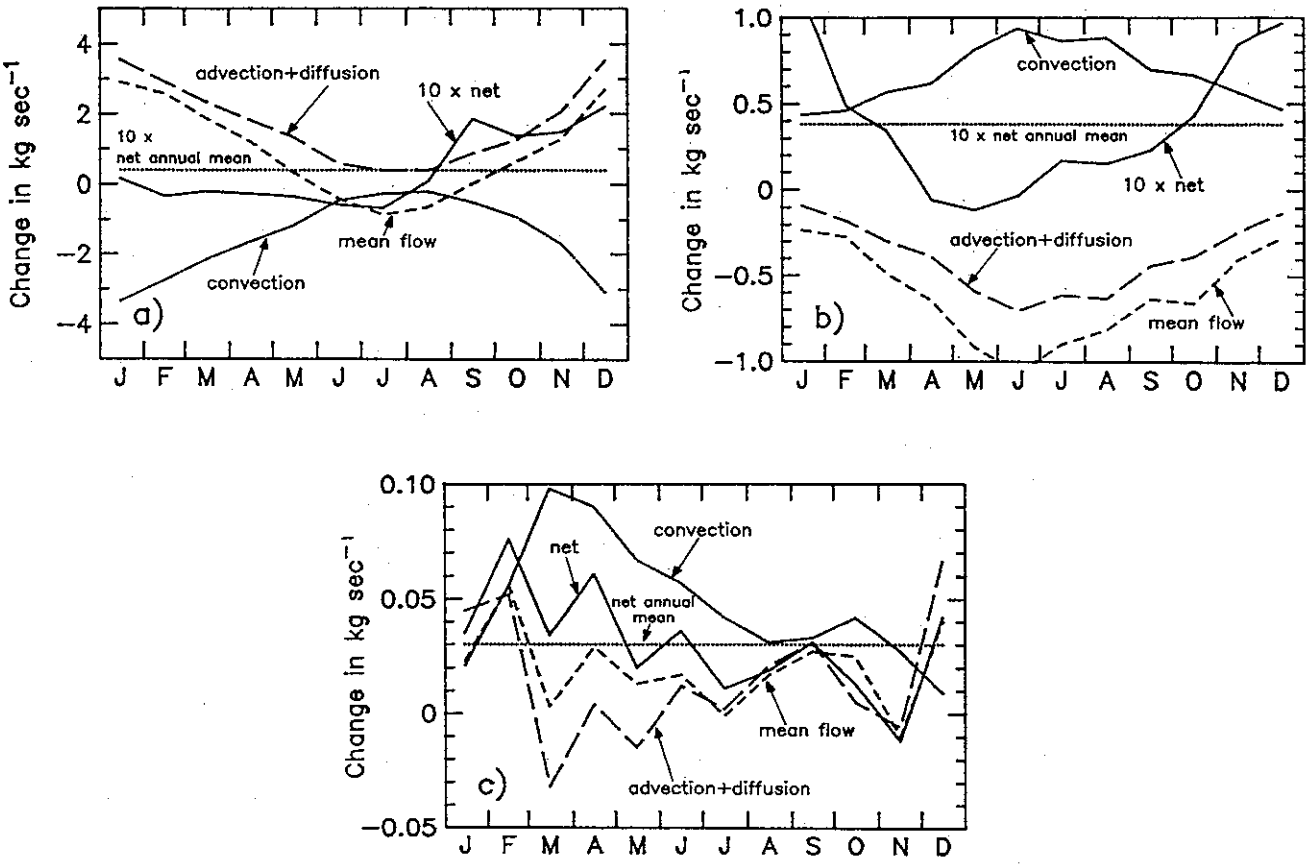

Fig. 29. Composition of the flux divergence for three zones 8° wide centered at (*a*) 12°N, (*b*) 12°S, and (*c*) 44°S and including the two lower σ layers (up to approximately 800 mbar). Solid lines represent the rate of net change in the tracer mass, with the annual mean marked by a dotted line. The net change comprises divergence of the advection and diffusion flux (long-dashed line), change by convection (dot-dashed line), and two components, emissions and loss, that were assumed constant throughout a year (not shown). Also shown is the contribution of the Hadley-like circulation (short-dashed line), representing divergence of the flux associated with zonally averaged velocities and concentrations (zonal mean computed every 8 hours). Note that in Figures 29*a* and 29*b* the net change is multiplied by 10. Also note the change of scale from Figure 29*a* to Figure 29*b* and to Figure 29*c*.

upper troposphere is at its maximum. At the same time the upper-to-lower troposphere gradient increases, leading to enhanced exchange by convection in March-May. These effects combine to cause an increase in concentrations during the first half of the year (see Figures 15 and 26).

7. Summary and Conclusions

The global three-dimensional distribution of OH was computed using a new parameterization of tropospheric photochemistry. We have developed a CTM for studying distributions of chemically reactive tracers. The CTM was applied to simulate the distribution of CH_3CCl_3 and to identify the features of the distribution, in addition to the long-term trends, that can be used to evaluate the computed OH. The model reproduces observed spatial and temporal variations in CH_3CCl_3, as defined by ALE/GAGE observations.

The computed OH field implies a global lifetime for CH_3CCl_3 of 5.5 years (obtained by relating the global burden of CH_3CCl_3 to the global loss, integrated using simulated three-dimensional distributions). Consistent with *Prinn et al.* [1987], the best fit to the observed long-term increase of CH_3CCl_3 is obtained with a lifetime of 6.2 years, implying that the model overestimates the global abundance of OH by 13%. This result is subject to uncertainties associated with data for global emissions and the absolute calibration of the ALE observations.

An independent assessment of the accuracy of the OH field was obtained by analyzing the annual cycles of CH_3CCl_3 at Tasmania and at Palmer, where the seasonal cycle is determined mainly by seasonal variations in OH. The best fit to the observed seasonal variation was found with the OH field scaled by a factor of 0.75±0.25, consistent with the estimate obtained from analysis of the long-term trend. This result is insensitive to the assumed emission scenario and to the absolute calibration. On the seasonal scale the whole distribution of CH_3CCl_3 south of about 25°S fluctuates as a coherent entity; therefore this estimate for the OH field applies to the concentration of OH averaged over the southern hemisphere from the subtropics to the pole (weighted by frequency of reaction with CH_3CCl_3).

It appears that the present simulation overestimates the global concentration of OH by about 15–25%. We expect that inclusion of reactions with nonmethane hydrocarbons could lead to a reduction in computed concentrations of OH by 10%–40%. Definite conclusions are not yet possible, however, given the deficiencies in the existing data base for nonmethane hydrocarbons, particularly for unsaturated species.

We showed that the observed latitudinal distribution of CH_3CCl_3 at present does not provide a constraint for the concentration of OH and that parameterization of tropical mixing based on data for CFCs [*Prather et al.* 1987] and ^{85}Kr [*Jacob et al.*, 1987] is consistent also with observations of CH_3CCl_3. The interhemispheric difference in the concentration of CH_3CCl_3 remained essentially in a steady state from 1978 to 1985, reflecting an approximately constant rate of emissions over this period.

Most of the observed seasonal variations in CFCs and CH_3CCl_3 can be reproduced assuming constant emissions throughout a year. Annual cycles of CH_3CCl_3 north of about 20°S are determined by seasonality of transport processes. The absolute amplitude (in pptv) of the chemical component in seasonal variations of CH_3CCl_3 is almost twice as high in the northern hemisphere as in the southern hemisphere, reflecting both higher concentrations of CH_3CCl_3 and higher concentrations of OH in the north.

If the global burden of CH_3CCl_3 continues to rise, the amplitude of the seasonal oscillation of CH_3CCl_3 (in pptv) south of about 25°S (where the seasonality is associated mainly with chemical loss) may be expected to increase proportionally. The predicted temporal change in the seasonal amplitude may be observable and could provide a useful check on the validity of the analysis presented here. If, on the other hand, emissions of CH_3CCl_3 are phased out, measurements of CH_3CCl_3 may offer new possibilities for testing OH models. After the cessation of release, we expect dynamically driven variations in CH_3CCl_3 diminish on a time scale of 1 year, whereas the concentration will decay on a longer time scale of 6 years. During this latter period the seasonal variations in northern mid-latitudes will reflect mainly the seasonality of OH, and therefore provide a test for OH models, as do variations in southern mid-latitudes at present. In addition, the tropical dent in the latitudinal distribution of CH_3CCl_3, caused by high concentrations of OH in the tropics, will also provide a measure of OH, since the effect of chemistry will no longer be obscured by interannual variations in transport and emissions. Consistent calibration of measurements and fine latitudinal resolution, including that in the equatorial region, will be required.

Our analysis suggests that monitoring programs should make a special effort to preserve information present in the frequency range 1–6 $year^{-1}$ (time scales 2-12 months), with particular attention to elimination of step changes associated with recalibration. If additional monitoring stations are to be considered in the future, sites in the subtropics would appear to be particularly interesting. Dynamical influences are complex for the region of Barbados and indeed for most of the north Atlantic. A station at Barbados alone can not provide a representation of northern subtropics sufficient for a comprehensive study of interhemispheric exchange or seasonality of transport processes; a northern Pacific subtropical site would add significantly to our understanding of the factors that influence the distribution of tracers in the tropics. A subtropical site at about 30°S would provide an important means for verifying OH models.

It is intended that future applications of the CTM will focus on global distributions of CO, CH_4, NO_x, and O_3. The chemical module developed for the present study allows for efficient computation of photochemical rates within a CTM simulation (as functions of changing tracer concentrations), essential for most of these studies. If chemical rates are recalculated at every time step, as many applications require, a CTM run using our parameterization of chemistry takes about twice the computer time of a calculation for a conservative tracer. Studies of global distributions of CO and CH_4 using the present CTM are currently in progress at Harvard and Goddard Institute for Space Studies.

APPENDIX A: INPUTS TO THE CHEMICAL MODULE

Data for temperature, cloud cover, and water vapor necessary for computing concentrations of OH and loss rates for CH_3CCl_3 were recorded in the GCM simulation as 5-day means. Zonal mean temperatures from the GCM agree with observations [*Oort*, 1983] within 2-3 K. Water vapor was taken from the GCM below 500 mbar, and was derived from observation above. In the CTM simulation, values for temperature, cloud cover, and water vapor below 500 mbar were updated every 5 days. Seasonal means were used for water vapor above 500 mbar. Distributions of O_3, CO, NO_t, and CH_4, described below, were derived from observation. Annual-mean profiles were used for NO_t and CH_4. Values for concentrations of O_3 and CO and for density of the O_3 column were updated every month.

Ozone. The locations of the stations used to derive the global distribution of tropospheric O_3 are given in Table A1 [*Logan*, 1985; *Oltmans and Komhyr*, 1986]. Mixing ratios were derived for each month, with a resolution of 15° for 75°S-15°N, and 7.5° for 15°N-75°N; these were converted to concentrations using standard atmospheres [*Cole and Kantor*, 1978]. Concentrations at latitudes greater than 75° were set equal to values at 75°. Recent data indicate that values of O_3 over the tropical continents and adjacent oceans are much higher than values over the mid-Pacific in certain months [*Delany et al.*, 1985; *Logan and Kirchhoff*, 1986; *Fishman and Larsen*, 1987; *Fishman et al.*, 1988; *Oltmans et al.*, 1988]. We allowed for higher O_3 over land at 0°-15°S, based on data from Natal, Brazil [*Logan and Kirchhoff*, 1986], but did not differentiate between land and ocean for latitudes northward of 15°N or southward of 30°S. Table A1 shows that data are sparse for the tropics and southern hemisphere.

TABLE A1. Ozone Data Used in the Chemical Tracer Model

Ozonesonde and Surface Stations	
75°N	Resolute; Barrow, Alaska.
60°N	Churchill; Bitumount, Alberta.
52.5°N	Goose Bay, Edmonton, Berlin; Bitumount
45-37.5°N	Hohenpeissenberg, Payerne, Biscarosse, Sapporo Bedford, Boulder, Cagliari, Wallops Island; Vermont, Wisconsin, Missouri, North Carolina.
30°N	Kennedy, Kagoshima, Grand Turk; Mauna Loa, Louisiana.
22.5°N	Hilo, Hawaii; Mauna Loa, Hawaii.
15°N	Average of 22.5°N and 0°.
0°	Oceans: Panama; Samoa. Land: Natal; Natal, Brazzaville, Congo.
15°S	Oceans: see Logan et al. [1981]. Land: same as land at 0°.
30-52.5°S	Aspendale; Cape Grim, Tasmania.
60°S	Average of Aspendale and Syowa.
75°S	Syowa.

The table gives the ozonesonde and surface stations used to derive the ozone climatology. The locations of stations, sources of data, and illustrations of the seasonal and vertical distributions are given by *Chatfield and Harrison* [1977*a*,*b*], *Logan* [1985], *Logan and Kirchhoff* [1986], *Oltmans and Komhyr* [1986], *Angle and Sandhu* [1986], and *Oltmans et al.* [1988].

Values for the overhead column of O_3 were taken from data obtained by the Total Ozone Mapping Spectrometer (TOMS). We used zonal monthly mean values derived from observations between January 1979 to December 1986 from Version 5.0 of the TOMS data processing [R. Stolarski, personal communication, 1987; *Kreuger et al.*, 1988]. Values for January and July are given in Table A2.

TABLE A2. Ozone Columns Used in the CTM.

Latitude	Jan.	July
90°N	...	324
84°N	...	327
76°N	...	329
68°N	394	333
60°N	382	346
52°N	386	348
44°N	365	330
36°N	320	309
28°N	275	298
20°N	253	289
12°N	247	282
4°N	251	273
4°S	256	264
12°S	264	261
20°S	270	270
28°S	280	288
36°S	294	318
44°S	312	336
52°S	333	335
60°S	339	319
68°S	327	295
76°S	316	...
84°S	309	...
90°S	306	...

Zonal-mean values are given for the center of each 8° latitude band in the CTM. The columns are given in Dobson units (equal to 2.69×10^{16} molecules cm^{-2} s^{-1}).

Nitrogen oxides. The CTM requires concentrations of a family of oxidized nitrogen species, NO_t ($NO + NO_2 + NO_3 + 2N_2O_5 + HNO_2 + HO_2NO_2$). Concentrations of NO_t, constant throughout a year, were chosen to reproduce representative profiles for NO [*Ridley et al.*, 1987; *Davis et al.*, 1987; *Torres and Buchan*, 1988; *Fehsenfeld et al.*, 1988]. The values of NO_t corresponding to observations of NO were derived using the full photochemical model (see Figure A1).

Methane and carbon monoxide. The methane field was assumed to be uniform in each hemisphere, with values of 1.7 ppm in the north and 1.6 ppm in the south. Values for CO in the CTM were based on measurements at a few sites in each hemisphere [*Khalil and Rasmussen*, 1983, 1984c; *Seiler et al.*, 1976, 1984; *Khalil and Rasmussen*, 1982; *Fraser et al.*, 1986], and from latitudinal surveys obtained using aircraft and ships [*Seiler*, 1974; *Heidt et al.*, 1980; *Seiler and Fishman*, 1981; *Schmidt et al.*, 1982]. Annual mean values for CO are given in Table A3 with latitude resolution of 10°. Uniform vertical profiles were used over the oceans, and over the continents above 2 km; surface values over land were calculated by scaling the midtropospheric values by the factors shown in Table A3. Monthly mean values were derived using the seasonal scaling factors in Table A4 for latitudes 30°-90°; seasonal factors for 0°-30° were interpolated from the values in Table A4 and a value of 1.0 at the equator.

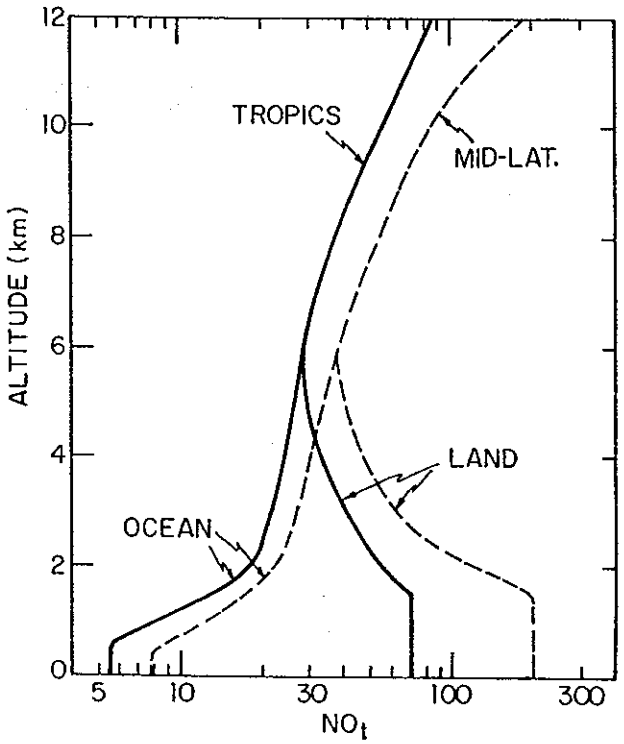

Fig. A1. Vertical profiles of NO_t (in ppt) used in the CTM, for ocean and land. The mid-latitude profiles were used for 90°-30°N, and the tropical profiles were used for 30°N-90°S.

Water vapor. Zonal mean concentrations of H_2O are within about 20% of observed values [*Oort*, 1983] in the lower troposphere. The specific humidity in the model tends to be too low below 700 mbar, and too high above, particularly in the tropics (see Figure A2). Model values for the upper troposphere (above 400 mbar) are too high by over a factor of 2, based on comparisons with data given by *Oort* [1983] and H. J. Mastenbrook [see *Logan et al.*, 1981]. The specific humidity at 500 mbar and above was specified, using the global radiosonde network [*Oort*, 1983] at 500 mbar and more limited data above 500 mbar: Mastenbrook's observations at Trinidad (10°N, 22 profiles), Washington D. C. (38°N, 116 profiles) [see *Logan et al.*, 1981, Figure 4], and Thule (76°N, 3 profiles), and 60 aircraft flights over Southern England (51°N) reported by *Cluley and Oliver* [1978].

TABLE A3. CO Latitudinal Distribution

Latitude	Mixing Ratio, ppb	Land Scaling Factor
90°- 60°N	136	1.0
55°N	136	1.2
45°N	130	1.3
35°N	124	1.2
25°N	118	1.2
15°N	113	1.2
5°N	100	1.2
5°S	86	1.2
15°S	72	1.2
20°- 90°S	65	1.0

TABLE A4. CO Seasonal Scaling Factors

Month	Northern Hemisphere	Southern Hemisphere
January	1.10	0.79
February	1.18	0.76
March	1.25	0.80
April	1.30	0.87
May	1.13	0.94
June	0.91	1.02
July	0.82	1.09
August	0.72	1.16
September	0.78	1.22
October	0.85	1.25
November	0.94	1.14
December	1.02	0.97

These values were used for latitudes > 30°. For lower latitudes, the scaling factors were interpolated linearly in latitude between the value at 30° and a value of 1. at the equator.

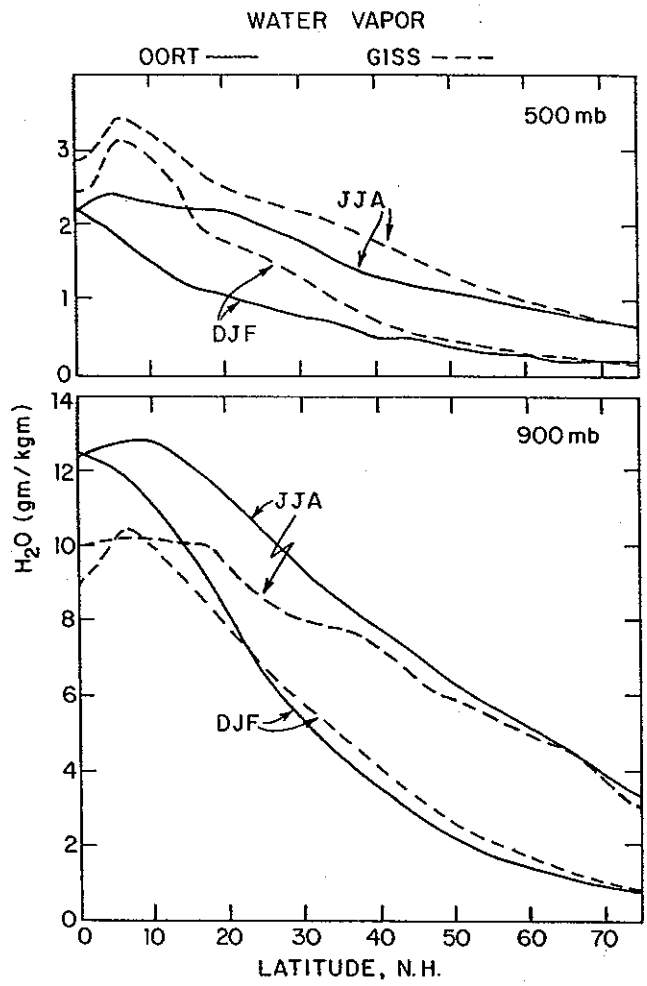

Fig. A2. Comparison of zonal mean values for specific humidity from the GCM (dashed) and from *Oort* [1983] (solid). Results are shown for summer and winter for 900 and 500 mbar.

APPENDIX B: INPUTS FOR SIMULATIONS OF THE DISTRIBUTION OF CH_3CCl_3

Stratospheric loss of CH_3CCl_3. The present CTM has two layers in the stratosphere, corresponding approximately to pressure intervals from 70 to 10 mbar and from 150 to 70 mbar. This resolution is sufficient for most applications when the distribution in the troposphere is of main interest. *Prather et al.* [1987] described an approach allowing for computation of the stratospheric loss rate, sufficiently accurate for the current study. The stratospheric loss is represented as a first-order loss process. Values for the loss frequencies are obtained from a one-dimensional photochemical model. Table B1 presents the resulting frequencies as a function of season and latitude at 15° intervals.

TABLE B1. Stratospheric Loss Frequency for CH_3CCl_3

	Latitude					
Month	0°	15°	30°	45°	60°	75°
	0-70 mbar					
January	0.746	0.450	0.206	0.292	0.119	0.000
April	0.830	0.697	0.410	0.400	0.206	0.109
July	0.688	0.729	0.668	0.498	0.409	0.272
October	0.860	0.744	0.465	0.272	0.183	0.085
	70-150 mbar					
January	0.104	0.048	0.013	0.002	0.000	0.000
April	0.128	0.099	0.043	0.013	0.006	0.002
July	0.094	0.109	0.098	0.062	0.042	0.043
October	0.132	0.107	0.055	0.025	0.013	0.005

Units are $year^{-1}$.

Emissions of CH_3CCl_3. There are no known natural sources for CH_3CCl_3. Independent estimates for production and sales of CH_3CCl_3 have been made by the principal manufacturing companies, Dow Chemical Company and Imperial Chemical Industries, PLC, (ICI); these estimates agree within 1%. We used sales data provided by P. Midgely, ICI (private communication, 1987), and assumed that 94% of annual sales are released to the atmosphere in the same year, following *Prinn et al.* [1983]. Annual releases are given in Table B2 for 1978-1986. Our estimate for the total release in 1978-1985 is within 1% of that of *Prinn et al.* [1987] and within 2% of recently published data for production of CH_3CCl_3, based on an audit of the manufacturers [*Midgely*, 1989].

Consumption patterns of CH_3CCl_3 are not well known, especially outside North America, Japan, and Western Europe. Following *Prather et al.*, [1987] we used electric power consumption as a surrogate for industrial activity to construct a global release pattern for CH_3CCl_3. Weighting factors that relate CH_3CCl_3 emissions to power consumption are given in Table B3. These factors are the same as those used for CFC-11 by *Prather et al.*, [1987] with the exception of the factor for Western Europe and Australia, and that for Japan. The fraction of CH_3CCl_3 released in each semi-hemisphere (90°-30°, 30°-0°) is the same as that given by industry sources for 1979-1985 [*Prinn et al.*, 1987], with the exception that the CTM allows for U.S. emissions south of 30°N

TABLE B2. Annual Emissions of CH_3CCl_3

Year	Emission, 10^9 g
1978	488.8
1979	544.5
1980	544.8
1981	540.2
1982	509.5
1983	520.6
1984	551.3
1985	582.5
1986	581.9

TABLE B3. Scaling Factors for Electric Power Release Grid

Region	Factor
United States and Canada	6
Western Europe and Australia	4
Japan	7
Rest of the world	2

These factors were used to scale electric power consumption, as given by *Prather et al.*, [1987, Table C2].

(in Florida) while industry estimates do not. About 3% of emissions are released in the southern hemisphere. This fraction has fluctuated from 2.7% to 3.1% in the period 1979-1986 (P. Midgley, private communication, 1988). We assumed that the release pattern was constant over this period.

Initial conditions. The simulations of CH_3CCl_3 were performed for the period of 6 years, starting at a model time of January 1, 1979. The field of initial concentrations was obtained in a special 1 year initialization run. For that run, uniform tropospheric concentrations of 100 and 72 ppt were assumed for northern and southern hemispheres, respectively, for January 1, 1978. Mixing ratios in the stratospheric layers were reduced by factors of 0.67 and 0.25, relative to tropospheric values. These factors were derived from observed stratospheric profiles [*World Meteorological Organization*, 1982, 1986]. Emissions for the initialization run were assumed 490×10^6 kg y^{-1}. Computed concentrations for January 1, 1979, were scaled by an uniform factor, to give a global burden of CH_3CCl_3 of $2{,}007 \times 10^6$ kg.

Acknowledgments. We are indebted to R. G. Prinn, D. R. Cronn, and P. J. Fraser for providing unpublished data. We thank D. Jacob, J. Yatteau, and A. Plumb for enlightening discussions. We are grateful to I. Tovbina, A. Johnson, and E. Gottlieb for help in analyzing the data, and to C. Demore and J. Rollet for editorial assistance. This work was supported by NASA grant NAG5-719, NSF grant ATM84-13153, and EPA grant R814535010 to Harvard University, and by Division of Applied Sciences, Harvard University.

REFERENCES

Angle, R. P., and H. S. Sandhu, Rural ozone concentrations in Alberta, Canada, *Atmos. Environ.*, *20*, 1221-1228, 1986.

Balkanski, Y. J., and D. J. Jacob, Transport of continental air to the subantarctic Indian Ocean, *Tellus*, *42*, 62-75, 1990.

Balkanski, Y. J., D. J. Jacob, R. A. Arimoto, and M. A. Kritz, General circulation model simulations of ^{222}Rn transport across the North Pacific, *Eos Trans. AGU*, *70*, 1024, 1989.

Chatfield, R., and H. Harrison, Tropospheric ozone, 1, Evidence for higher background values, *J. Geophys. Res.*, *82*, 5965-5968, 1977*a*.

Chatfield, R., and H. Harrison, Tropospheric ozone, 2, Variations along a meridional band, *J. Geophys. Res.*, *82*, 5969-5976, 1977*b*.

Chatfield, C., Simple descriptive techniques chap. 2, in *The Analysis of Time Series, III ed.*, pp. 12-30, Chapman and Hall, London 1984.

Chameides, W. L., and A. Tan, The two-dimensional diagnostic model for tropospheric OH: An uncertainty analysis, *J. Geophys. Res.*, *86*, 5209-5223, 1981.

Cluley, A. P., and M. J. Oliver, Aircraft measurements of humidity in the low stratosphere over southern England 1972-1976, *Q. J. R. Meteorol. Soc.*, *104*, 511-526, 1978.

Cole, A. E., and A. J. Kantor, Air Force Reference Atmospheres. Air Force Surveys in Geophysics, 382, *Rep. AFGL-TR-78-0051*, Air Force Geophys. Lab., Bedford, Mass., 1978.

Cronn, D. R., W. L. Barnesberger, F. A. Menzia, S. F. Waylett, A. S. Waylett, T. W. Ferrara, H. M. Howard, and E. Robinson, Atmospheric trace gas trends at Palmer Station, Antarctica: 1982-1985, *Geophys. Res. Lett.*, *13*, 1272-1275, 1986.

Crutzen, P. J., and L. T. Gidel, A two-dimensional photochemical model of the atmosphere, 2, The tropospheric budgets of the anthropogenic chlorocarbons CO, CH_4, CH_3Cl, and the effect of various NO_x sources on tropospheric ozone, *J. Geophys. Res.*, *88*, 6641-6661, 1983.

Cunnold, D. M., F. Alyea, N. Phillips, and R. Prinn, A three-dimensional dynamical-chemical model of atmospheric ozone, *J. Atmos. Sci.*, *32*, 170-194, 1975.

Cunnold, D. M., F. N. Alyea, and R. G. Prinn, A methodology for determining the atmospheric lifetime of fluorocarbons, *J. Geophys. Res.*, *83*, 5493-5500, 1978.

Cunnold, D. M., R. G. Prinn, R. A. Rasmussen, P. G. Simmonds, F. N. Alyea, C. A. Cardelino, A. J. Crawford, P. J. Fraser, and R. D. Rosen, Atmospheric lifetime and annual release estimates for $CFCl_3$ and CF_2Cl_2 from 5 years of data, *J. Geophys. Res.*, *91*, 10,797-10,817, 1986.

Davis, D. D., J. D. Bradshaw, M. O. Roders, S. T. Sandholm, and S. KeSheng, Free tropospheric and boundary layer measurements of NO over the central and eastern North Pacific ocean, *J. Geophys. Res.*, *92*, 2049-2047, 1987.

Delany, A. C., P. J. Crutzen, P. Haagensen, S. Walters, and A. F. Wartburg, Photochemically produced ozone in the emission from large scale tropical vegetation fires, *J. Geophys. Res.*, *90*, 2425-2593, 1985.

Dunker, A. M., The reduction and parameterization of chemical mechanisms for inclusion in atmospheric reaction-transport models, *Atmos. Environ.*, *20*, 479-486, 1986.

Durbin, J., Trend elimination for the purpose of estimating seasonal and periodic components of time-series in *Proceedings of Symposium on Time Series Analysis held at Brown University, June 11-14*, edited by M. Rosenblatt, Wiley, New York, 1962.

Ehhalt, D. H., J. Rudolph, F. Meixner, and U. Schmidt, Measurements of selected C_2-C_5 hydrocarbons in the background troposphere: Vertical and latitudinal variations, *J. Atmos. Chem.*, *3*, 29-52, 1985.

Enting, I. G., The seasonal cycle of atmospheric CO_2 in the Australian region: A signal processing analysis in *Atmospheric Program, Baseline 85*, edited by B. W. Forgan and P. J. Fraser, Bureau of Meteorology, Melbourne, Australia, pp. 19-25, 1987.

Fehsenfeld, F. C., D. D. Parrish, and D. W. Fahey, The measurement of NO_x in the nonurban troposphere in *Proceedings of the NATO Advanced Research Workshop on Regional and Global Ozone and its Environmental Consequences*, edited by I. S. A. Isaksen, *NATO ASI Ser. C*, *227*, pp. 185-216, D. Reidel, Hingham, Mass., 1988.

Fishman, J., and J. C. Larsen, Distribution of total ozone and stratospheric ozone in the tropics: implications for the distribution of tropospheric ozone, *J. Geophys. Res.*, *92*, 6627-6634, 1987.

Fishman, J., C. E. Watson, and J. C. Larsen, The distribution of total ozone, stratospheric ozone, and tropospheric ozone at low latitudes deduced from satellite data sets, in *Ozone in the Atmosphere*, edited by R. D. Bojkov and P. Fabian, pp. 411-414, A. Deepak Publishing, Hampton, Va., 1989.

Fraser, P. J., and N. Derek, Atmospheric halocarbons and nitrous oxide,

1982-1985 in *Atmospheric Program, Baseline 85*, edited by B. W. Forgan and P. J. Fraser, Bureau of Meteorology, Melbourne, Australia, 1987.

Fraser, P. J., N. Derek, R. O'Brien, R. Shepherd, R. A. Rasmussen, and A. J. Crawford, Atmospheric halocarbons and nitrous oxide, 1976-1984, in *Atmospheric Program, Baseline 1983-1984*, edited by R. J. Francey and B. W. Forgan, Bureau of Meteorology, Melbourne, Australia, pp. 43-49, 1985*a*.

Fraser, P. J., N. Derek, R. O'Brien, R. Shepherd, R. A. Rasmussen, A. J. Crawford, and L. P. Steele, Intercomparison of halocarbon and nitrous oxide measurements, 1976-1984, in *Atmospheric Program, Baseline 1983-1984*, edited by R. J. Francey and B. W. Forgan, Bureau of Meteorology, Melbourne, Australia, pp. 17-26, 1985b.

Fraser, P. J., P. Hyson, R. A. Rasmussen, A. J. Crawford, and M. A. K. Khalil, Methane, carbon monoxide and methylchloroform in the southern hemisphere, *J. Atmos. Chem., 4*, 3-42, 1986.

Fung, I., K. Prentice, E. Matthews, J. Lerner, and G. Russell, Three-dimensional tracer model study of atmospheric CO_2: response to seasonal exchanges with the terrestrial biosphere, *J. Geophys. Res., 88*, 1281-1294, 1983.

Golombeck, A,. and R. G. Prinn, A global three-dimensional model of the circulation and chemistry of $CFCl_3$, CF_2Cl_2,CH_3CCl_3 , CCl_4, and N_2O, *J. Geophys. Res., 91*, 3985-4001, 1986.

Hansen, J., G. Russell, D. Rind, P. Stone, A. Lacis, S. Lebedeff, R. Ruedy, and L. Travis, Efficient three-dimensional global models for climate studies: Models I and II, *Mon. Weather Rev., 111*, 609-662, 1983.

Heidt, L. E., J. P. Krasnec, R. A. Lueb, W. H. Pollock, B. E. Henry, and P. J. Crutzen, Latitudinal distributions of CO and CH_4 over the Pacific, *J. Geophys. Res., 85*, 7329-7336, 1980.

Hunt, B. G., Experiments with a stratospheric general circulation model. III. Large-scale diffusion of ozone including photochemistry, *Mon. Weather Rev., 97*, 287-306, 1969.

Hunt, B. G. and S. Manabe, Experiments with a stratospheric general circulation model. II. Large scale diffusion of tracers in the stratosphere. *Mon. Weather Rev., 96*, 503-539, 1968.

Jacob, D. J., and M. J. Prather, Radon-222 as a test of convective transport in a general circulation model, *Tellus, 42*,118-134,1990.

Jacob, D. J., M. J. Prather, S. C. Wofsy, and M. B. McElroy, Atmospheric distribution of ^{85}Kr simulated with a general circulation model, *J. Geophys. Res., 92*, 6614-6626, 1987.

Khalil, M. A. K., and R. A. Rasmussen, Gaseous tracers of Arctic haze, *Environ. Sci. Technol., 17*, 157-164, 1983.

Khalil, M. A. K., and R. A. Rasmussen, Methylchloroform: Global distribution, seasonal cycles, and anthropogenic chlorine, *Chemosphere, 13*, 789-800, 1984a.

Khalil, M. A. K., and R. A. Rasmussen, The atmospheric lifetime of methylchloroform (CH_3CCl_3), *Tellus, 36B*, 317-332, 1984b.

Khalil, M. A. K., and R. A. Rasmussen, Increasing trend of carbon monoxide in the Earth's atmosphere, *Science, 224*, 54-56, 1984c.

Kley, D., J. W. Drummond, M. McFarland, and S. C. Liu, Tropospheric profiles of NO_x, *J. Geophys. Res., 86*, 3153-3161, 1981.

Krueger, A. J., M. R. Schoeberl, and R. S. Stolarski, The 1987 antarctic ozone hole: A new record low, *Geophys. Res. Lett., 15*, 1365-1368, 1988.

Levy, H., II, and W. J. Moxim, Simulated global distribution and deposition of reactive nitrogen emitted by fossil fuel combustion, *Tellus, 41B*, 256-271, 1989.

Levy, H., II, J. D. Mahlman, and W. J. Moxim, Tropospheric N_2O variability, *J. Geophys. Res., 87*, 3061-3080, 1982.

Levy, H., II, J. D. Mahlman, W. J. Moxim, and S. C. Liu, Tropospheric ozone: The role of transport, *J. Geophys. Res., 90*, 3753-3772, 1985.

Levy, H., II, and W. J. Moxim, Fate of U.S. and Canadian combustion nitrogen emissions, *Nature, 328*, 414-416, 1987.

Logan, J. A., Tropospheric ozone: Seasonal behavior, trends, and anthropogenic influence, *J. Geophys. Res., 90*, 10,463-10,482, 1985.

Logan, J. A., and V. W. H. Kirchhoff, Seasonal variations of tropospheric ozone at Natal, Brazil, *J. Geophys. Res., 91*, 7875-7881, 1986.

Logan, J. A., M. J. Prather, S. C. Wofsy, and M. B. McElroy, Atmospheric chemistry: Response to human influence, *Phil. Trans. R. Soc. London, Ser. A, 290*, 187-234, 1978.

Logan, J. A., M. J. Prather, S. C. Wofsy, and M. B. McElroy, Tropospheric chemistry: A global perspective, *J. Geophys. Res., 86*, 7210-7254, 1981.

Lovelock, J. E., Methyl chloroform in the troposphere as an indicator of OH radical abundance, *Nature, 267*, 32-33, 1977.

Mahlman, J. D., and W. J. Moxim, Tracer simulation using a global general circulation model: Results from a mid-latitude instantaneous source experiment, *J. Atmos. Sci., 35*, 1340-1378, 1978.

Mahlman, J.D., H. Levy, II, and W.J.Moxim, Three-dimensional tracer structure and behavior as simulated in two ozone precursor experiments, *J. Atmos. Sci., 37*, 655-685, 1980.

Makide, Y., and F. S. Rowland, Tropospheric concentrations of methylchloroform, CH_3CCl_3, in January 1978 and estimates of atmospheric residence times for hydrohalocarbons, *Proc., Nat. Acad. Sci. U.S.A., 78*, 5933-5973, 1981.

Marsden, A. R., Jr., M. Frenklach, and D. D. Reible, Increasing the computational feasibility of urban air quality models that employ complex mechanisms, *JAPCA, 37*, 370-376, 1987.

Midgley, P.M., The production and release to the atmosphere of 1,1,1-trichloroethane (methyl chloroform), *Atmos. Environ., 23*, 2663-2665, 1989.

NASA, Chemical kinetics and photochemical data for use in stratospheric modeling, Eval. 7, *JPL Publ., 85-37*, 1985.

Oltmans, S. J., and W. D. Komhyr, Surface ozone distributions and variations for 1973-1984 measurements at the NOAA Geophysical Monitoring for Climatic Change baseline observatories, *J. Geophys. Res., 91*, 5229-5236, 1986.

Oltmans, S. J., W. D. Komhyr, P. R. Franchois, and W. A. Matthews, Tropospheric ozone: variations from surface and ECC ozonesonde observations, in *Ozone in the Atmosphere*, edited by R. D. Bojkov and P. Fabian, pp. 539-543, A. Deepak Publishing, Hampton, Va., 1989.

Oort, A. H., Global atmospheric circulation statistics, 1958-1973, *Natl. Oceanic Atmos. Admin. Pap. 14*, 1983.

Pearman, G. I., and D. J. Beardsmore, Atmospheric carbon dioxide measurements in the Australian region: Ten years of aircraft data, *Tellus, 36B*, 1-24, 1984.

Perner, D., U. Platt, M. Trainer, G. Hubler, J. Drummond, W. Junkermann, J. Rudolph, B. Schubert, A. Volz, and D. H. Ehhalt, Measurements of tropospheric OH concentrations: A comparison of field data with model predictions, *J. Atmos. Chem., 5*, 185-216, 1987.

Pinto, J. P., Y. L. Yung, D. Rind, G. Russell, J. A. Lerner, J. E. Hansen and S. Hameed, A general circulation model study of atmospheric carbon monoxide, *J. Geophys. Res., 88*, 3691-3702, 1983.

Platt, U., M. Rateike, W. Junkermann, J. Rudolph, and D. H. Ehhalt, New tropospheric OH measurements, *J. Geophys. Res., 93*, 5159-5166, 1988.

Plumb, A. R., and D. D. McConalogue, On the meridional structure of long-lived tropospheric constituents, *J. Geophys. Res., 93*, 15,897-15,913, 1988.

Plumb, A. R., and J. D. Mahlman, The zonally averaged transport characteristics of the GFDL general circulation/transport model, *J. Atmos. Sci., 44*, 298-327, 1987.

Prather, M. J., Continental sources of halocarbons and nitrous oxide, *Nature, 317*, 221-225, 1985.

Prather, M. J., Numerical advection by conservation of second-order moments, *J. Geophys. Res., 91*, 6671-6681, 1986.

Prather, M. J., European sources of halocarbons and nitrous oxide: Update 1986, *J. Atmos. Chem., 6*, 375-406, 1988.

Prather, M. J., M. B. McElroy, and S. C. Wofsy, Reductions in ozone at high concentrations of stratospheric halogens, *Nature, 312*, 227-231, 1984.

Prather, M. J., M. B. McElroy, S. C. Wofsy, G. Russell, and D. Rind, Chemistry of the global troposphere: Fluorocarbons as tracers of air motion, *J. Geophys. Res., 92*, 6579-6613, 1987.

Prinn, R. G., R. A. Rasmussen, P. G. Simmonds, F. N. Alyea, D. M. Cunnold, B. C. Lane, C. A. Cardelino, and A. J. Crawford, The atmospheric

lifetime experiment, 5, results for CH_3CCl_3 based on 3 years of data, *J. Geophys. Res.*, *88*, 8415-8426, 1983.

Prinn, R., D. Cunnold, R. Rasmussen, P. Simmonds, F. Alyea, A. Crawford, P. Fraser, and R. Rosen, Atmospheric trends in methylchloroform and the global average for the hydroxyl radical, *Science*, *238*, 945-950, 1987.

Rasmussen, R. A., and M. A. K. Khalil, Atmospheric trace gases and Arctic haze at Point Barrow, pp.114-120 in *Geophysical Monitoring for Climatic Change*, edited by B. A. Bodhaine and J. M. Harriss, U.S. Dept. of Comm., Boulder, Col., 1982.

Rasmussen, R. A., and J. E. Lovelock, The atmospheric lifetime experiment, 2, Calibration, *J. Geophys. Res. 88*, 8369-8378, 1983.

Ridley, B. A., M. A. Carroll, and G. L. Gregory, Measurements of nitric oxide in the boundary layer and free troposphere over the Pacific Ocean, *J. Geophys. Res.*, *92*, 2025-2047, 1987.

Rudolph, J., Two-dimensional distribution of light hydrocarbons: results from the STRATOZ III Experiment, *J. Geophys. Res.*, *93*, 8367-8377, 1988.

Russell, G., and J. A. Lerner, A new finite differencing scheme for the tracer transport equation, *J. App. Meteorol.*, *20*, 1483-1498, 1981.

Schmidt, U., A. Khedim, F. J. Johnen, J. Rudolph, and D. H. Ehhalt, Two dimensional meridional distribution of CO, CH_4, N_2O, $CFCl_3$, and CF_2Cl_2 in the remote troposphere over the Atlantic ocean, paper presented at *The Second Symposium on the Nonurban Troposphere*, Am. Meteorol. Soc., Boston, Mass., 1982.

Seiler, W., The cycle of atmospheric CO, *Tellus*, *26*, 118-135, 1974.

Seiler, W., and J. Fishman, The distribution of carbon monoxide and ozone in the free troposphere, *J. Geophys. Res.*, *86*, 7255-7265, 1981.

Seiler, W., H. Giehl, and H. Ellis, A method for monitoring of background CO and first results of continuous CO registrations on Mauna Loa Observatory, *Spec. Environ. Rep. 10*, 31-39, World Meteorol. Org., Geneva, 1976.

Seiler, W., H. Giehl, E. Brunke, and E. Halliday, The seasonality of CO and abundance in the southern hemisphere, *Tellus*, *368*, 219-231, 1984.

Singh, H. B., Atmospheric halocarbons: Evidence in favor of reduced hydroxyl radical concentrations in the troposphere, *Geophys. Res. Lett.*, *4*, 241-244, 1977*a*.

Singh, H. B., Preliminary estimation of average tropospheric HO concentrations in the northern and southern hemispheres, *Geophys. Res. Lett.*, *4*, 453-456, 1977*b*.

Singh, H. B., W. Viezee, and L. J. Salas, Measurements of selected C_2-C_5 hydrocarbons in the troposphere: Latitudinal, vertical, and temporal variations, *J. Geophys. Res.*, *93*, 15,861-15,878, 1988.

Spivakovsky, S. C. Wofsy, and M. J. Prather, A numerical method for parameterization of atmospheric chemistry: Computation of tropospheric OH, *J. Geophys. Res.*, this issue.

Thompson, M. L., I. G. Enting, G. I. Pearman, and P. Hyson, Interannual variation of atmospheric CO_2 concentration, *J. Atmos. Chem.*, *4*, 125-155, 1986.

Torres, A. L., and H. Buchan, Tropospheric nitric oxide measurements over the Amazon basin, *J. Geophys. Res.*, *93*, 1396-1406, 1988.

World Meteorological Organization, The stratosphere 1981: Theory and measurements, *WMO Rep. 11*, Geneva, 1982.

World Meteorological Organization, Atmospheric ozone 1985: Assessment of our understanding of the processes controlling its present distribution and change, *WMO Rep. 16*, Geneva, 1986.

Wofsy, S. C., Temporal and latitudinal variations of stratospheric trace gases: A critical comparison between theory and experiment, *J. Geophys. Res.*, *83*, 364-378, 1978.

J. A. Logan, M. B. McElroy, C. M. Spivakovsky, S. C. Wofsy, and R. Yevich, Division of Applied Sciences and Department of Earth and Planetary Sciences, Harvard University, Cambridge, MA 02138.

M. J. Prather, Goddard Institute of Space Studies, NASA, 2880 Broadway, New York, NY 10025.

(Received September 15, 1989;
revised June 11, 1990;
accepted June 11, 1990.)